

TURBULENT CONVECTION IN STELLAR INTERIORS. I. HYDRODYNAMIC SIMULATION

CASEY A. MEAKIN^{1,2} AND DAVID ARNETT¹

Draft version October 22, 2018

ABSTRACT

We describe the results of three-dimensional (3D) numerical simulations designed to study turbulent convection in the stellar interiors, and compare them to stellar mixing-length theory (MLT). Simulations in 2D are significantly different from 3D, both in terms of flow morphology and velocity amplitude. Convective mixing regions are better predicted using a *dynamic boundary condition* based on the bulk Richardson number than by purely local, static criteria like Schwarzschild or Ledoux. MLT gives a good description of the velocity scale and temperature gradient for a mixing length of $\sim 1.1H_p$ for shell convection, however there are other important effects that it does not capture, mostly related to the dynamical motion of the boundaries between convective and nonconvective regions. There is asymmetry between up and down flows, so the net kinetic energy flux is not zero. The motion of convective boundaries is a source of gravity waves; this is a necessary consequence of the deceleration of convective plumes. Convective "overshooting" is best described as an elastic response by the convective boundary, rather than ballistic penetration of the stable layers by turbulent eddies. The convective boundaries are rife with internal and interfacial wave motions, and a variety of instabilities arise which induce mixing through in process best described as turbulent entrainment. We find that the rate at which material entrainment proceeds at the boundaries is consistent with analogous laboratory experiments as well as simulation and observation of terrestrial atmospheric mixing. In particular, the normalized entrainment rate $E = u_E / \sigma_H$, is well described by a power law dependence on the bulk Richardson number $Ri_B = \Delta b L / \sigma_H^2$ for the conditions studied, $20 \lesssim Ri_B \lesssim 420$. We find $E = A Ri_B^{-n}$, with best fit values, $\log A = 0.027 \pm 0.38$, and $n = 1.05 \pm 0.21$. We discuss the applicability of these results to stellar evolution calculations.

Subject headings: stars: evolution - stars: nucleosynthesis - massive stars - hydrodynamics - convection - g-modes

1. INTRODUCTION

We have simulated three-dimensional (3D), turbulent, thermally-relaxed, nearly adiabatic convection (high Péclet number). Such flow is relevant to deep convective regions in stars (i.e., to most stellar mass which is convective, but not mildly sub-photospheric and surface regions). We simulate oxygen shell burning on its natural time scale, and core hydrogen burning driven at 10 times its natural rate. The simulations develop a robust quasi-steady behavior in a statistical sense, with significant intermittency. We analyze this statistical behavior quantitatively, and compare it to predictions of astrophysical mixing length theory (Böhm-Vitense 1958). Mixing-length Theory (MLT) gives a good representation of many aspects of convection, but omits others (especially wave generation and mass entrainment) which are related to the dynamical behavior of stably stratified layers adjacent to the convection.

In Section 2 we briefly summarize some results of the study of turbulent entrainment in geophysics, to prepare the reader for its appearance in our astrophysical simulations. This process is not included in the standard approach to stellar evolution (Cox & Guili 1968; Clayton 1983; Kippenhahn & Weigert 1990; Hansen & Kawaler 1994). In Section 3 we discuss our numerical and theoretical tools. In Section 4 we present our simulations of

oxygen shell burning, which attain a thermal steady state (this is possible because of the rapidity of nuclear heating and neutrino cooling). In Section 5 we discuss a less advanced burning stage, core hydrogen burning, which we are able to examine with the use of an artificially enhanced hydrogen burning rate (by a factor of ten). We find that the behavior is similar to the oxygen burning shell, suggesting that our results may have broad application for stellar evolution. In Section 6 we compare our results to the assumptions of MLT, and in Section 7 we show that our results lead to a simple model of turbulent entrainment, an effect not in MLT nor in standard stellar evolutionary calculations.

This paper is the first in a series. In subsequent papers, we incorporate the "empirical" convection model developed in this paper into the TYCHO stellar evolution code (Young & Arnett 2005) and begin to assess its influence on stellar evolution, on nucleosynthetic yields, and on the structure of supernova progenitors.

2. TURBULENT ENTRAINMENT

The presence of a turbulent layer contiguous with a stably stratified layer is common in both astrophysical and geophysical flows. Turbulence in a stratified media is often sustained by strong shear flows or thermal convection and bound by a stabilizing density interface. Over time, the turbulent layer "diffuses" into the stable layer and the density interface recedes, thus increasing the size of the mixed, turbulent region. The basic features of this *turbulent entrainment problem* are illustrated in Figure 1. The rate at which the density interface recedes into

Electronic address: cmeakin@as.arizona.edu, darnett@as.arizona.edu

¹ Steward Observatory, University of Arizona, Tucson AZ

² FLASH Center, University of Chicago, Chicago IL

the stable layer $u_E = \partial r_i / \partial t$ is called the entrainment rate, and its dependence on the parameters characterizing the turbulent and the stable layers has been the subject of numerous experimental and theoretical studies. It is generally ignored in stellar evolutionary studies.

Experimental studies have mostly been of “mixing box” type which involves a tank of fluid with a turbulent layer and a density stratified layer. The turbulence is generated by thermal convection or an oscillating wire mesh, and density stratification imposed by either a solute or thermal gradient (Turner 1980). Complementary to these shear-free mixing box models are shear driven-models. Shear-driven turbulence experiments involve either a recirculation track which propels one layer of fluid above a stationary layer, or a rotating plate in contact with the fluid that drives a circulation in the upper layer. Shear instabilities sustain a turbulent mixed layer in the overlying fluid which then entrains fluid from the lower, stationary layer (Kantha et al. 1977; Strang & Fernando 2001). In all of these laboratory experiments, a variety of flow visualization techniques are used to study both the overall entrainment rate u_E and the physical mechanisms which underly the entrainment process.

One of the primary conclusions of these studies is that the entrainment rate depends on a Richardson number, which is a dimensionless measure of the “stiffness” of the boundary relative to the strength of the turbulence. In shear-free turbulent entrainment the bulk Richardson number,

$$Ri_B = \frac{\Delta b L}{\sigma^2}, \quad (1)$$

is most commonly studied. Here, Δb is the buoyancy jump across the interface, σ is the r.m.s. turbulence velocity adjacent the interface, and L is a length scale for the turbulent motions often taken to be the horizontal integral scale of the turbulence at the interface. The relative buoyancy is defined by the integral,

$$b(r) = \int_{r_i}^r N^2 dr \quad (2)$$

where N is the buoyancy frequency defined by,

$$N^2 = -g \left(\frac{\partial \ln \rho}{\partial r} - \frac{\partial \ln \rho}{\partial r} \Big|_s \right). \quad (3)$$

The entrainment coefficient E is the interface migration speed u_e normalized by the R.M.S. turbulent velocity at the interface $E = u_E / \sigma$, and is generally found to obey a power law dependence on Ri_B ,

$$E = ARi_B^{-n}. \quad (4)$$

The exponent is usually found to lie in the range $1 \lesssim n \lesssim 1.75$ and has been the subject of many theoretical studies of the entrainment process. Dimensional analysis suggests that Ri_B should be the controlling parameter, so long as microscopic diffusion plays a minor role (Phillips 1966). Basic energetic arguments in which the rate of change of potential energy due to mixing is assumed to be proportional to the turbulent kinetic energy available at the interface leads to an exponent of $n = 1$ (e.g. Linden 1975). This same power law exponent has

also been derived for models of the growth of the planetary boundary layer due to turbulent entrainment by penetrative convection (Stull 1973; Tennekes 1974; Stull 1976a; Sorbjan 1996).

The normalization of the entrainment coefficient A has been found to vary significantly between the various laboratory and field studies conducted, with recent values found in the range $0.1 < A < 0.5$ (e.g. Stevens & Bretherton 1999). The discrepancy among the normalization constants has been called the ‘A-dilemma’ (Bretherton et al. 1999). A review (up to 1991) of experimental measures of the parameters in the entrainment law of equation 4 are tabulated in Fernando (1991) and a recent review of entrainment models used in the atmospheric sciences is discussed by Stevens (2002).

The experimental and theoretical models discussed above are generally motivated by geophysical problems, but are directly relevant to the conditions found in stellar interiors. The bulk Richardson numbers which characterize stellar convective boundaries fall within the same parameter range ($10 < Ri_B < 500$), and the background stratification possesses a similar buoyancy structure, so that it is interesting to learn from the geophysical models and compare to the stellar case.

3. THE NUMERICAL TOOLS

3.1. 1D Stellar Evolution

The hydrodynamic simulations which we study in this paper are of two distinct phases in the evolution of a $23M_\odot$ supernova progenitor: main sequence core convection, and convective oxygen shell burning. The initial conditions for the multi-dimensional simulations are taken from one-dimensional stellar models evolved with the TYCHO stellar evolution code. TYCHO (Young & Arnett 2005) is an open source code³. A choice of standard 1D stellar evolution procedures are used. The mixing length theory as described in Kippenhahn & Weigert (1990) is used with instantaneous mixing of composition in the convectively unstable regions. The limits of the convection zones are determined using the Ledoux criterion, which incorporates the stabilizing effects of composition gradients. Semiconvective mixing has been turned off. Nuclear evolution is followed with a 177 element network using the rates of (Rauscher & Thielemann 2000). Opacities are from (Iglesias & Rogers 1996) and (Alexander & Ferguson 1994) for high and low temperature regimes, respectively. The solar abundance of Grevesse & Sauval (1998) are used. Although more recent abundance determinations have been made (Asplund et al. 2005) the impact on the stellar structure of the models presented here is small, and minor variations in the abundances have a negligible influence on the development of the hydrodynamic flow.

3.2. Multi-Dimensional Reactive Hydrodynamics with PROMPI

The core of our multi-dimensional hydrodynamics code is the solver written by Fryxell, Müller, & Arnett (1989) which is based on the direct Eulerian implementation of PPM (Colella & Woodward 1984) with generalization to non-ideal gas equation of state (Colella & Glaz

³ <http://chandra.as.arizona.edu/~dave/tycho-intro.html>

1985). This code solves the Euler equations, to which we add nuclear reactions and radiative diffusion through an operator-split formulation. The complete set of combus- tive Euler equations, including diffusive radiative trans- fer, can be written in state-vector form,

$$\frac{\partial \mathbf{Q}}{\partial t} + \nabla \cdot \mathbf{\Phi} = \mathbf{S}, \quad (5)$$

with the *state vector*

$$\mathbf{Q} \equiv \begin{bmatrix} \rho \\ \rho \mathbf{u} \\ \rho E \\ \rho X_l \end{bmatrix}, \quad (6)$$

the *flux vector*

$$\mathbf{\Phi} \equiv \begin{bmatrix} \rho \mathbf{u} \\ \rho \mathbf{u} \mathbf{u} + p \\ (\rho E + p) \mathbf{u} + \mathbf{F}_r \\ \rho X_l \mathbf{u} \end{bmatrix}, \quad (7)$$

and the *source vector*

$$\mathbf{S} \equiv \begin{bmatrix} 0 \\ \rho \mathbf{g} \\ \rho \mathbf{u} \cdot \mathbf{g} + \rho \epsilon_{net} \\ R_l \end{bmatrix}, \quad (8)$$

where $E = E_I + E_K$ is the total energy per gram consisting of internal and kinetic energy components, and ρ , p , \mathbf{u} , \mathbf{g} , and T are the density, pressure, velocity, gravi- tational force field and temperature. The net energy source term due to nuclear reactions and neutrino cool- ing is $\epsilon_{net} = \epsilon_{burn} + \epsilon_{cool}$, and the time rate of change of composition X_l due to nuclear reactions is denoted R_l . The radiative flux is $\mathbf{F}_r = -k_r \nabla T$, with radiative “conductivity” $k_r = 4acT^3/(3\kappa_R \rho)$ and Rosseland mean opacity, κ_R . Self gravity is implemented assuming the interior mass at each radius is distributed with spheri- cal symmetry. The mass interior to the inner boundary of the hydrodynamics grid is adopted from the TYCHO stellar model.

The stellar models, which are calculated on a finely meshed Lagrangian grid, are linearly interpolated onto the Eulerian hydrodynamics grid taking into account the sub-grid representation of mass used in the PPM scheme. Mapping the models leads to small discrepancies in hydrostatic equilibrium. An equilibration to hydrostatic balance occurs through the excitation and then damping of low amplitude, standing, predominantly radial pres- sure waves within the computational domain. These low amplitude waves, which are well described by the lin- earized wave equation, have a negligible affect on the convective flow.

To save computational resources, we simulate care- fully chosen subregions of the star. Thus, these calcu- lations are local models of convection in the *box in a star* tradition. The advantage of local convection mod- els is that higher effective resolution can be used than is currently possible in global circulation models. This approach, however, precludes investigation of the lowest order modes of flow, and we do not yet include rotation or magnetic fields which are best studied using global domains. The boundary conditions used are periodic in

angular directions, and stress-free reflecting in the radial direction.

Our simulation code, dubbed PROMPI, has been adapted to parallel computing platforms using domain decomposition and the sharing of a three zone layer of boundary values and uses the MPI message passing li- brary to manage interprocess communication.

4. OXYGEN SHELL BURNING

We have evolved a $23M_\odot$ stellar model with the TY- CHO code to a point where oxygen is burning in a shell which overlies a silicon-sulfur rich core. Approximately 60% of the oxygen fuel available for fusion has been de- pleted at the time we begin the hydrodynamic simula- tion, when the star is $\sim 2 \times 10^7$ yrs from the zero age main sequence. Carbon, helium, and hydrogen burn- ing shells are also present contemporaneously at larger radii in the classic “onion skin” structure (Hoyle 1946). In one of the models presented here (ob.2d.e), which is also discussed in Meakin & Arnett (2006a), we adopt an outer radius that encompasses both the oxygen and car- bon burning shells. In this paper, however, we focus our analysis on the oxygen shell burning convection zone and the stable layers which bound it.

The oxygen shell burning model affords us the oppor- tunity to study a thermally relaxed model because the thermal balance is determined by the very large neutrino cooling rates rather than the much lower radiative diffu- sion timescale (Arnett 1996, ch.11). Neutrinos dominate the energy balance in the stable layers so that the stellar structure and the nature of convection are determined by the interplay between nuclear burning and neutrino emission (Aufderheide 1993; Arnett 1972). The effects of radiative diffusion are both unresolved and energeti- cally unimportant during these evolutionary phases, and has not been included in the oxygen shell calculations for computational efficiency.

The radial profile of the simulated region is presented in Figure 2. The temperature and density profiles be- tray the complex structure of the model, including the narrow burning shell that resides at the very base of the convection zone which is coincident with the tempera- ture peak. The initial extent of the convection zone can be identified by the plateau in oxygen mass frac- tion at $0.43 < r_9 < 0.72$ (where $r_9 = r/10^9$ cm). Char- acteristic of shell burning regions, the entropy gradient is quite steep at the boundaries of the convection zone and gives rise to peaks in the buoyancy frequency at those locations. The initial location of the upper con- vective boundary is coincident with a small stable layer at $r \sim 0.72 \times 10^9$ cm, which is overwhelmed by the con- vective flow that develops in the simulation (see §4.1). A new boundary forms where the buoyancy frequency again becomes stabilizing at $r \gtrsim 0.8 \times 10^9$ cm. This mix- ing is shown in the change in ^{16}O abundance (Figure 2, top right) after 400s.

In Table 1 we list the 25 nuclei used in our network. This network reproduces to within 1% the energy gener- ation of the full 177 element network used to evolve the one-dimensional TYCHO model for the simulated condi- tions, including oxygen and carbon burning shells. Dur- ing carbon burning the dominant reactions are $^{12}\text{C}(^{12}\text{C}, \alpha)^{20}\text{Ne}$ and $^{12}\text{C}(^{12}\text{C}, p)^{23}\text{Na}$, leaving an ash of ^{20}Ne , ^{23}Na , protons and alpha-particles. ^{20}Ne is photodis-

integrated through the $^{20}\text{Ne}(\gamma, \alpha)^{16}\text{O}$ reaction. The dominant reactions during oxygen burning are $^{16}\text{O}(^{16}\text{O}, \alpha)^{28}\text{Si}$, $^{16}\text{O}(^{16}\text{O}, \text{p})^{31}\text{P}$, and $^{16}\text{O}(^{16}\text{O}, \text{n})^{31}\text{S}$, leaving an ash of predominantly ^{28}Si and ^{32}S . Neglecting the non-alpha chain species ^{23}Na , ^{31}P and ^{31}S can affect the net energy generation rate during carbon and oxygen burning by a factor of a few under the conditions studied here. The reaction rates, including $^{12}\text{C}(\alpha, \gamma)^{16}\text{O}$, are from Rauscher & Thielemann (2000).

Nuclear evolution is time advanced using the same reaction network subroutines as the TYCHO code and uses implicit differencing (Arnett 1996). We include cooling by neutrino-antineutrino pair emission, denoted ϵ_{cool} , which result from photo, pair, plasma, bremsstrahlung, and recombination processes (Beaudet et al. 1967; Itoh et al. 1996).

The Helmholtz equation of state code of Timmes & Swesty (2000) is used to represent the ion and electron pressure with an arbitrary degree of electron degeneracy. With our 25 nuclei network, the initial conditions are thermodynamically consistent with the initial TYCHO model to better than a few percent at all radii after mapping to the hydrodynamics grid.

We calculate oxygen shell burning models in two and three dimensions. Our baseline model, labeled ob.2d.c, is a 90° wedge embedded in the equatorial plane with radii encompassing the oxygen burning convective shell and two stable bounding layers. The effects of dimensionality on the oxygen burning convective shell are explored with a three-dimensional model ob.3d.B which has an angular extents of $(27^\circ)^2$. The influence of the upper boundary was studied with model ob.2d.e, which includes the overlying carbon burning convective shell as well (additional details concerning this model are presented in Meakin & Arnett (2006a)). A preliminary resolution study is undertaken with model ob.2d.C which uses the same domain limits but twice the linear resolution of the baseline model. Properties of the oxygen shell burning models presented in this paper are summarized in Table 2.

4.1. The Correct Mixing Boundary

Convection is initiated through random low-amplitude (0.1%) perturbations in density and temperature applied to a region in the center of the convectively unstable layer on a zone by zone basis. (Two additional simulation models with the same characteristics as ob.2d.c were calculated which used perturbations with a larger amplitudes and (1%), and a low order mode distribution. The development of the convective flow was found to be insensitive to these differences.) The role played by the perturbations is to break the angular symmetry of the initial model, and seed rising and sinking plumes whose growth is driven by nuclear burning, neutrino cooling, and the slightly superadiabatic background gradient imprinted in the initial TYCHO model. As the plumes rise they penetrate the original convective boundary which was determined in the TYCHO code using the Ledoux criterion. The initial evolution of the flow is presented in a time series of snapshots in Figure 3; the light yellow contour shows the initial outer convective boundary.

The location of the initial outer boundary can be seen as a small bump in the initial profile of the buoyancy frequency presented in Figure 2 at radius $r \sim .72 \times 10^9$ cm. The reason the boundary is stable in the 1D model but

did not survive in the multi-D simulation is because of the local nature of the Ledoux criterion used. This can be appreciated by the fact that although the buoyancy frequency at this location is positive, and hence locally stable to convective turnover, the *buoyancy jump* across this region is very small $\Delta b \sim 3 \times 10^6$ cm/s² compared to the turbulent kinetic energy in the adjacent flow, by which it is easily overwhelmed. This type of inconsistency can be relatively easily removed from 1D simulations by using a parameter akin to the bulk Richardson number (eq. [1]) to characterize convective boundaries in place of the Ledoux or Schwarzschild criteria. For the original outer boundary $Ri_B \lesssim 1$, a condition under which a boundary is expected to mix on an advection timescale, akin to the expansion of turbulence into a homogenous medium.

The relationship between Ri_B and the traditional Schwarzschild and Ledoux criteria can be appreciated by writing the buoyancy frequency in terms of the well known "nablas" used in stellar evolution,

$$N^2 = \frac{g\delta}{H_P} \left(\nabla_{ad} - \nabla_s + \frac{\varphi}{\delta} \nabla_\mu \right) \quad (9)$$

where $\nabla = (d \ln T / d \ln p)$, ∇_s is the gradient of the stellar background, ∇_{ad} is the gradient due to an adiabatic displacement, $\nabla_\mu = (d \ln \mu / d \ln p)$ is the mean molecular weight gradient, and the thermodynamic derivatives are $\delta = -(d \ln \rho / d \ln T)$ and $\varphi = (d \ln \rho / d \ln \mu)$. Therefore, the Ledoux criteria is simply,

$$N^2 > 0. \quad (10)$$

The Schwarzschild criteria is the same, but with the stabilizing effect of the mean molecular weight gradient ∇_μ neglected. For comparison, the bulk Richardson number can be written $Ri_B \sim N^2 h L / \sigma^2$, where h is some measure of the boundary width. A convective boundary will start to become stabilizing when,

$$N^2 \gtrsim \sigma^2 / (hL). \quad (11)$$

This latter criteria is based on a finite threshold for stability which takes into account the strength of the convective turbulence. Additionally, the bulk Richardson number is more than a simple stability criteria; it is also an indicator of the rate at which boundary erosion will proceed. We conclude that the correct criterion for determining the extent of a convective zone is neither the Ledoux nor the Schwarzschild criterion, which are both static, linear, and local criteria, but a *dynamic boundary condition*, based on the bulk Richardson number, which we will discuss in more detail in §7.

4.2. Time Evolution

The rich dynamics taking place at the convective boundary are apparent in the time evolution of the 3D flow presented in Figure 4, which provides a global view of the evolution. The upper panel shows the evolution in time and radius of the oxygen abundance gradient, represented by a colormap in which light is large and dark is small. At the beginning of the simulation (far left) the colors are smooth as the turbulence has not yet developed. The light line near the bottom of the panel is the lower boundary of the convective shell, where oxygen is separated from the silicon-sulfur core below. The

short horizontal band at $r \sim 0.72 \times 10^9$ cm is the initial weakly stable convective boundary discussed above; it is overwhelmed in the first 100 seconds by convection. After ~ 300 seconds the abundance distribution has approached a quasi-steady state, with slow growth of the convective region. The bottom of the convection zone moves downward, but at a much slower rate than the upper boundary moves outward. The mottled appearance in the convection zone is due to the ingestion of new oxygen entrained from above, followed by turbulent mixing. At the top boundary of the convection zone an oscillatory behavior can be seen, and in the overlying stable region wave motions are apparent.

The lower panel in Figure 4 shows the radial profile of the kinetic energy, which illustrates a major feature of the convection: intermittency. While these simulations are well described by a statistical steady state over a few convective turnover times, at any instant the fluctuations are significant. The flow is episodic, with bursts of activity followed by lulls. The bursts in kinetic energy in the convection zone are seen to induce wave trains in both the upper and lower stable layers. Characteristic of g-modes, the phase velocity (orientation of the wave crests) is orthogonal to the group velocity (direction of energy transport) in these wave trains, which can be seen by comparing the composition and kinetic energy profiles.

4.3. Quasi-Steady Oxygen Shell Burning Convection

Following the transient readjustment of the outer convective boundary, the oxygen burning convective shell attains a quasi-steady character. In Figure 5 we present the time evolution of the integrated internal, gravitational, and kinetic energy. The energy is calculated by forming horizontal averages of the flow properties and then assuming a full spherical geometry. The gravitational energy contribution from material on the computational grid is calculated according to,

$$E_G \equiv \int \frac{GM(r)dM}{r}, \quad (12)$$

where the mass increment is $dM = 4\pi r^2 \langle \rho \rangle$, and the integral is taken over the radial limits of the grid.

The total kinetic energy levels off in all of the models by $t \sim 300$ s. The 2D models are characterized by a much larger overall kinetic energy. The total kinetic energy settles down to a slow increase as the oxygen shell evolves; this is true for both 2D and 3D.

The radial profile of the r.m.s. velocity fluctuations are presented in Figure 6 for the 2D and 3D models. The velocity fluctuation amplitudes in all of the 2D models are higher than the 3D model by a factor of ~ 2 . The 2D models also assume a significantly different radial profile than the 3D model, with a flow structure that is dominated by large convective vortices which span the depth of the convection zone. The signature of these large eddies is apparent in the horizontal velocity components, as well as the fairly symmetric shape of the radial velocity profile within the convection zone. The velocity components in the 3D model reveal an up and down flowing circulation with horizontal deflection taking place in a fairly narrow layer at the convective boundaries.

Although significant differences exist between 2D and 3D models, the 2D models are found to be in good agree-

ment with each other to the extent that the statistics have converged, which are calculated over the time period $t \in [300, 450]$ s. The time period for calculating statistics was limited by the model ob.2d.C, which was only run as far as $t \sim 450$ s. The agreement among the 2D models shows that the outer boundary condition (tested by model ob.2d.e) and the grid resolution (tested by model ob.2d.C) are not playing a decisive role in determining the overall structure of the flow, at least in these preliminary tests. The agreement in overall velocity amplitude in the upper stable layer in model ob.2d.e indicates that the stable layer velocity amplitudes are not strongly affected by the details of the modes that are excited in that region. This gives credence to the analysis in (Meakin & Arnett 2006b) which assumes that the stable layer velocity amplitudes are determined by the dynamical balance between the convective ram pressure and the wave induced fluctuations.

The convective turnover times $t_c = 2\Delta R/v_{conv}$ for the 2D models are all of order $t_c \sim 40$ s, and they span between 10 and 55 convective turnovers. The turnover time for the 3D model is $t_c \sim 103$ s, and the model spans approximately 8 convective turnovers.

4.4. Stable Layer Dynamics During Shell Burning

In both the 2D and 3D models, the stably stratified layers are characterized by velocity fluctuations throughout their extents (Figure 6). These fluctuations are the signature of g-modes which are excited by the convective motions. In the 2D model, the amplitudes of the stable layer velocity fluctuations are higher. In the lower stable layer, the 2D models also have a much smaller ratio of horizontal to radial velocity amplitude. The velocity amplitude ratio is roughly proportional to the ratio of the mode frequency and buoyancy frequency, $v_r/v_\perp \approx \omega/N$ (Press 1981), so that the waves excited in the 2D model are of lower frequency. The velocity ratios in the upper stable layer are comparable between the 2D and 3D models, though the 2D amplitudes are higher by a factor of ~ 2 .

During late burning stages, multiple concentric convective shells form which are separated by stably stratified layers. These intervening stable layers act as resonating cavities for g-modes that are excited by the turbulent convection. In Meakin & Arnett (2006a) it was shown that the stable layer motions in model ob.2d.e can be decomposed into individual g-modes that are well described by the linearized non-radial wave equation (Unno et al. 1989). Meakin & Arnett (2006b) showed that a good estimate for the amplitudes of the wave motions (and the associated thermodynamic fluctuations) in both the 2D and 3D models can be made by assuming that the pressure fluctuations associated with the g-modes balance the ram pressure of the turbulent convection. In the latter paper, a single mode (frequency and horizontal scale) was assumed, based on integral properties of the turbulence (convective turnover time, and mixing length scale). In this section we present the spectrum of motions present in the stable layers and turbulent regions for the more realistic 3D model.

For a given background structure, a spectrum of eigenmodes exist which are solutions to the non-radial wave equation and boundary conditions. Individual modes can be uniquely identified by a horizontal wavenumber index

l and oscillation frequency ω . In Figure 7, $l - \omega$ diagrams are presented for the convection zone, and the two bounding stable layers. The individual $l - \omega$ components have been isolated through Fourier transforms of a time sequence of the simulation data.

Several modal components or "branches" can be identified in the stable layer diagrams (left and right panels). These include: (1) p-modes, seen as a series of points at the lowest l values that extend to high frequencies; (2) g-modes, which appear as ridges that are bound above by the buoyancy frequency; and (3) f-modes, which appears as a ridge separating the g- and p-modes. The f-modes are interfacial waves, and are most prominently seen in the lower-boundary diagram at a radius $r = 0.4 \times 10^9$ cm. The f-mode signature is due to interfacial waves running along the convective boundary at $r \sim 0.43 \times 10^9$ cm, where there is a spike in buoyancy frequency.

In the convection zone, the spectrum is dominated by power at low temporal and spatial frequencies. This strong non-modal convection signature is also present, though at lower amplitude, in the stable layers. This "turbulence" spectrum can be seen extending from the lower left corner of the diagrams. This same feature was also present in the simulations of He-shell burning by Herwig et al. (2006).

5. CORE CONVECTION

Are the hydrodynamic features of oxygen shell burning of more general applicability? To investigate this, we examined core convection during hydrogen burning. Because of the long thermal time scale for radiative diffusion in such stars, we focus on the hydrodynamic behavior of a model in which the inner boundary provides a driving luminosity about ten times larger than natural. This allows us to simulate the convection with our compressible hydrodynamics code; an anelastic method (if multi-fluid) would allow this to be done in the star's natural time scale. While our calculation is not thermally relaxed on a Helmholtz-Kelvin time scale, it does relax dynamically, and provides some clue as to the convective behavior.

We have previously evolved a $23 M_{\odot}$ star onto the main sequence with TYCHO, to an age of 2.4×10^5 yrs, at which point hydrogen is burning in a convective core. The model is then mapped onto the PROMPI hydrodynamics grid for simulation. This model represents an early point in main sequence evolution, in which the core hydrogen content has been depleted by only 1.7% ($X_{core} = 0.689$, $X_{init} = 0.701$, $\Delta X = 0.012$). The inner radius of the simulation was chosen such that the convectively unstable region covers ~ 1 pressure scale height (convective cores are usually only of order a pressure scale height because of the divergence of the scale height towards the stellar center). The entire domain covers ~ 5 pressure scale heights and ~ 3.3 density scale heights. The density contrast across the computational domain is ~ 30 with a contrast of ~ 2 across the convectively unstable region.

The radial profile of the simulated region is presented in Figure 8 including the run of temperature, density, composition, buoyancy frequency, and relative buoyancy. The entropy jump at the edge of the convective core, due to the fuel-ash separation, gives rise to a buoyancy jump (spike in buoyancy frequency).

The equation of state for the main sequence model is

well described by an ideal gas with radiation pressure component. The ratio of gas to total pressure lies in the range $0.85 < \beta < 0.95$, with an increasing contribution from radiation pressure as the stellar center is approached. A single composition representing hydrogen has been evolved to keep track of nuclear transmutation and the mean molecular weight of the plasma. A metallicity of $Z = 0.01879$ has been used to represent the additional 175 species in the initial TYCHO model and helium is calculated according to $Y = 1 - (X + Z)$, where X is the self consistently evolved hydrogen mass fraction.

The luminosity due to nuclear burning in the computational domain is a small fraction of the total stellar luminosity (2.4%) which is dominated by burning in the inner regions of the core and $L_{tot} = 7.8 \times 10^4 L_{\odot}$. Core burning is incorporated into the simulation as an input luminosity at the inner boundary of the computational domain.

The Kelvin-Helmholtz timescale for this model is $t_{KH} \sim 10^5$ years, which is many orders of magnitude longer than the dynamical timescales that are feasible to simulate. Additionally, the small luminosity of the star produces a convective velocity scale that is very subsonic ($M \sim 10^{-3}$). Since we are not interested in the thermal relaxation of the model, we have boosted the input luminosity by a factor of 10 to increase the velocity scale of the flow. This was necessary because our fully compressible code is limited by the sound crossing time. (An anelastic or low-mach number method would be ideal for simulating this core convection flow at the natural velocity scale.)

Radiation transport is treated in the diffusion limit. Opacities approximated by Thompson scattering, which agrees well with the OPAL opacities (Iglesias & Rogers 1996) used in the 1D TYCHO model for the region simulated. The effects of radiative diffusion, however, are found to be unresolved in the current simulation (with the diffusion time across a single zone $\tau_{rad} = \Delta^2/k_{rad} \gg t_{conv}$, with grid zone size Δ) and therefore energy transport in the convection zone occurs primarily on the sub-grid level due to numerical diffusion. This is a high Péclet number simulation.

A 2D and a 3D model have been calculated. The simulated wedges have angular extents of 30° in both the polar and azimuthal directions and are centered on the equator to avoid zone convergence problems near the poles. This minimal angular domain size was chosen by calculating models of increasing angular size in 2D domains until the flow pattern converged. The angular domain size used in the present simulations encompasses a large convective roll in 2D. Smaller 2D domains were found to distort the convective roll while domains larger by integer multiples contained proportionally more rolls of the same flow amplitude and morphology. The boundary conditions in the radial direction are reflecting and stress free, and periodic conditions are used in both angular directions. The grid zoning, domain limits, and simulation run times are summarized in Table 3 for the 2D and 3D models.

5.1. Quasi-Steady Core Convection

Convection is initiated through random low-amplitude (0.1%) perturbations in density and temperature applied as in the oxygen shell simulation. In order to save com-

puting time, the 3D model was initiated on a domain one quarter as large in azimuthal angle which was then tiled four times in angle once convective plumes began to form. The initial development of the flow in the 3D model is presented in Figure 9 as a time sequence of velocity iso-surfaces. The turbulent structure of the convective flow, as well as the excitation of internal waves which radiate into the overlying stably stratified layer, are clearly illustrated. A comparison of the flow morphology between the 2D and 3D models is presented in Figure 10. The 2D convective flow is much more organized and laminar, and is dominated by a single large convective cell while the 3D convection is composed of many smaller scale plume-like structures and is more obviously turbulent. In both models the stably stratified regions are rife with internal waves excited by the convection.

The 3D convective flow attains a quasi-steady character after approximately 6×10^5 s, or approximately two convective turnovers. The evolution of the internal, gravitational, and total kinetic energy components on the computational grid for the 2D and 3D models, are presented in Figure 11 and are calculated in the same way as for the oxygen burning model.

In both the 2D and 3D models, the total kinetic energy fluctuates in times with excursions from the mean as larger $\delta E_K / \overline{E_K} \sim 0.4$ in 3D and $\delta E_K / \overline{E_K} \sim 0.6$ in 2D. The kinetic energy in the 2D model grows on a slightly longer timescale, and achieves a steady character after $\sim 10^6$ s, at which time the kinetic energy growth rate tapers off. The total energy is conserved to better than $\sim 0.2\%$ for both the 2D and 3D flows by the end of the calculation.

The r.m.s. velocity fluctuations are presented in Figure 12 for the 2D and 3D models. The resultant flows in both the 2D and 3D models are similar to that found for the oxygen shell burning model. The velocity amplitudes are higher in 2D by a factor of ~ 5 (see axis scale in Figure 12), and the flows are dominated by large eddies spanning the depth of the convective region. The horizontal deflection of matter is also found to occur in a much narrower region in the 3D model. The hard-wall lower boundary of the 3D model is characterized by an even narrower horizontal flow, probably due to the absence of a stable layer which is host to g-modes.

The time averaged convective flow velocity for the 3D model is $v_c \approx 2.8 \times 10^5$ cm/s. The turnover time is $t_c = 2\Delta R/v_c \approx 3.2 \times 10^5$ s, and the simulation spans approximately 5 convective turnovers. The peak velocity fluctuation is $v_{peak} \sim 2 \times 10^6$ cm/s, corresponding to a peak Mach number of $M \sim 0.03$, and the maximum density fluctuations within the convective flow are $\sim 0.02\%$, which is of order M^2 as expected for low Mach number thermal convection (Gough 1969). The time averaged convective flow velocity in the 2D model is $v_c \approx 1.3 \times 10^6$ cm/s, and the convective turnover time for this model is $t_c \approx 7 \times 10^4$ s. The simulation spans 1.5×10^6 s which is ~ 21 convective turnovers. The peak velocity fluctuation in the 2D model is comparable to that in the 3D simulation, with $v_{peak} \sim 2 \times 10^6$ cm/s and the peak density fluctuations is a little more than twice that found in the 3D model, $\sim 0.05\%$. The turnover times and convective velocity scales are summarized in Table 3.

5.2. The Stable Layer Dynamics Overlying the Convective Core

As in the oxygen shell burning model, the stably stratified layers in the core convection models are characterized by velocity fluctuations throughout. Similar to shell burning, the 2D stable layer velocity amplitudes are larger and have a smaller radial to horizontal component ratio $v_r/v_\perp \approx \omega/N$ compared to the 3D flow.

The stable layer motions in the core convection simulation are predominantly resonant modes, which compare well to the analytic eigenmodes of the linearized wave equation, and are analogous to those discussed for the oxygen shell burning model. The region outside the convective core will act as a resonant cavity, with the outer boundary at the location where the buoyancy frequency and Lamb frequency cross.

The amplitudes of the internal waves excited will

be determined by the ram pressure of the turbulence at the convective boundary. In Figure 13 the ram pressure and horizontal r.m.s. pressure fluctuations are presented for the 3D model, and can be seen to balance at the interface between the convective core and the stably stratified layer. Using this condition of pressure balance, Meakin & Arnett (2006b) estimate the amplitudes of the excited internal wave velocities and the induced thermodynamic fluctuations and find this to be in good agreement with the oxygen shell burning simulations. The relationship between the density fluctuations, the convective velocity scale, and the stellar structure (i.e., N and g) was found to be,

$$\frac{\rho'}{\langle \rho \rangle} \sim M_c^2 + \frac{v_c N}{g}. \quad (13)$$

That this proportionality holds in the core convection model as well, where fluctuation amplitudes are lower than those in the oxygen shell burning model by an order of magnitude, is illustrated in Figure 14, which presents the buoyancy frequency and density fluctuation profiles for the boundary region. The measured density fluctuation and the value calculated according to equation 13 compare remarkably well, with $\rho'/\langle \rho \rangle \sim 0.12\%$.

6. SIMULATIONS AND MIXING LENGTH THEORY

In this section we compare our 3D oxygen shell burning simulation results to the mixing length theory of convection. We choose to compare this particular simulation since it represents the most physically complete model in our suite of calculations, both in terms of dimensionality and thermal evolution. Unless otherwise specified, the time period over which averaging is performed on the simulation data is $t \in [400, 800]s$, which is approximately 4 convective turnovers. We find that this period is sufficiently long compared to the time evolution of the flow that average values are not affected appreciably by increases in the averaging time period.

6.1. Mixing Length Theory Picture

The basic picture underlying the mixing length theory, which is the standard treatment of convection used in one-dimensional stellar evolution modeling (see Cox & Guili 1968; Clayton 1983; Kippenhahn & Weigert 1990; Hansen & Kawaler 1994), is one in which large eddies are accelerated by an unstable temperature gradient and

advect across a certain distance until they suddenly lose their identity by turbulently mixing with the *background*. Energy is transported through this process because the envisioned turbulent *blobs* which are moving radially outward have a higher entropy at their formation location than the location in which they *dissolve*. The vertical extent over which large eddies retain their identity as they advect through a convection zone is a fundamental parameter in the mixing length theory. This *mixing length* Λ is generally taken to be a multiple of the local pressure scale height $\Lambda = \alpha_\Lambda H_p$.

Within this physical picture, the mixing length theory develops a relationship between the convective flux, the temperature gradient, the velocity scale, and the geometrical factors which describe the large scale eddies. The starting point in mixing length theory is the radial enthalpy flux, which is written in terms of fluctuations in the flow properties, and is taken to be (assuming a horizontally isobaric flow),

$$F_c = v_c \rho c_p T'. \quad (14)$$

The temperature fluctuations in mixing length theory are related to the temperature gradient and the distance traveled by,

$$T'/T = \left(\frac{\partial \ln T_e}{\partial r} - \frac{d \ln T_0}{dr} \right) \frac{\Lambda}{2} = (\Delta \nabla) \frac{1}{H_p} \frac{\Lambda}{2} \quad (15)$$

where the subscript "e" indicates properties of the large convective eddies and the dimensionless temperature gradient ∇ is used (see §4.1), and the difference between the gradient in the eddy as it moves and the averaged stellar background is written,

$$\Delta \nabla = (\nabla - \nabla_e).$$

The factor of 1/2 in equation 15 represents the idea that on average the large convective eddies have traversed about half a mixing length before reaching the current position. The velocity obtained by the convective eddy is computed by calculating the work done by the buoyancy force over a mixing length,

$$v_c^2 = g\beta(\Delta \nabla) \frac{\Lambda^2}{8H_p}. \quad (16)$$

Here again, the eddy is assumed to have been accelerated over half of a mixing length and an additional factor of 1/2 is incorporated on the right hand side to account for energy lost driving other flows, such as small scale turbulence and horizontal motions (e.g., note that the r.m.s. horizontal velocity is of the same order as the r.m.s. radial velocity in the simulation). The average convective flux can then be written,

$$F_c = \rho c_p T \sqrt{g\beta} \frac{\Lambda^2}{4\sqrt{2}H_p^{3/2}} (\Delta \nabla)^{3/2}. \quad (17)$$

The temperature gradient for the convecting material is found by assuming that eddies follow isentropic trajectories $\nabla_e = \nabla_{ad}$. Deviations from isentropic motion have been considered in the mixing length theory. In the case of strong radiative diffusion losses, the eddy geometry (in terms of the surface area to volume ratio) is an

important additional parameter since the eddies are envisioned to *leak* a fraction of their thermal energy over a mixing length distance. When local cooling dominates, either through radiative losses (in optically thin regions) or neutrino losses (such as in the present model), the geometry of the eddies is not important since energy escapes everywhere from the large eddies, not just at eddy "surfaces".

During the oxygen shell burning simulations being considered here, non-adiabatic losses are small over a convective turnover time and the convection is expected to be "efficient". A quantitative measure of convective efficiency is the Péclet number, which is the ratio of the energy loss timescale to the convective turnover timescale for the large eddies. In the current model, energy losses are dominated by neutrino cooling ϵ_ν . Therefore, we calculate an effective Péclet number using the following convective and neutrino-cooling timescales:

$$\tau_c \sim \frac{H_p}{v_c} \quad (18)$$

$$\tau_\nu \sim \frac{c_p T'}{T' \partial \epsilon_\nu / \partial T} = \frac{c_p T}{\epsilon_\nu} \left(\frac{\partial \ln \epsilon_\nu}{\partial \ln T} \right)^{-1} \quad (19)$$

$$Pe = \frac{\tau_\nu}{\tau_c} \sim \frac{v_c c_p T}{H_p \epsilon_\nu} \left(\frac{\partial \ln \epsilon_\nu}{\partial \ln T} \right)^{-1} \sim 10^4 \left(\frac{\partial \ln \epsilon_\nu}{\partial \ln T} \right)^{-1} \quad (20)$$

where characteristic values from the simulation have been used in equation 20, and the temperature dependence of the neutrino loss rates is $(\partial \ln \epsilon_\nu / \partial \ln T) \lesssim 9$. Therefore, the Péclet number for the convection is $Pe \gtrsim 10^3$, and we should expect the convection zone to be very nearly isentropic.

6.2. The Enthalpy Flux, Background Stratification, and Temperature and Velocity Fluctuations

The convective enthalpy flux measured in the simulation is presented in Figure 15. The spike at the bottom of the convection region and the slight dip at the top reflect the braking of convective motion at these boundaries. The enthalpy flux is calculated by performing time and horizontal averages on the flow. Mixing length theory, however, makes the assumption that the velocity and temperature fluctuations are perfectly correlated, so that horizontal averaging of fluctuations is comparable to products of the averages. This is not necessarily the case. To test the degree to which the velocity and temperature fluctuations are correlated we can calculate the correlation coefficient, α_E , defined in the following way:

$$F_c = \langle \rho c_p T' v'_c \rangle = \alpha_E \langle \rho c_p \rangle \langle T' \rangle \langle v'_c \rangle. \quad (21)$$

The fluctuations, T' and v'_c in equation 21 are taken to be the r.m.s. fluctuations in the simulation. The radial profile of α_E is shown in Figure 15. We find $\langle \alpha_E \rangle = 0.7 \pm 0.03$ averaged over the radial interval $r \in [0.5, 0.75] \times 10^9$ cm within the convection zone. A value smaller than unity indicates that the horizontal distribution of temperature and velocity fluctuations in the flow are not perfectly correlated. The degree of correlation, however, is found to be fairly uniform throughout the convection zone.

We next consider how well the velocity and temperature fluctuations are correlated with the local temperature gradient. In Figure 16 the temperature gradient of the horizontally averaged hydrodynamic model profile ∇_s as well as the adiabatic ∇_{ad} and the composition-corrected (Ledoux) gradient $\nabla_{Led} = \nabla_{ad} + \varphi/\beta \times \nabla_\mu$, are presented. The super-adiabatic temperature profile of the stellar background $\Delta\nabla = \nabla_s - \nabla_{ad}$ is presented in the right panel of Figure 16. While the convection zone is found to have a super-adiabatic profile throughout, it is very small ($\Delta\nabla \lesssim 10^{-3}$). This confirms the efficiency of the convection, in accord with our estimate for Pé. Stability is maintained in the upper boundary layer by the composition gradient, where we have $\nabla_{ad} < \nabla_s < \nabla_{Led}$.

In order to assess the validity of the mixing length theory temperature and velocity fluctuation amplitudes given by equations 15 and 16 we calculate the correlation coefficients α_T and α_v which are defined by,

$$T'/T = (\Delta\nabla)\alpha_T \quad (22)$$

and

$$v_c = \frac{\alpha_v}{2} \sqrt{g\beta(\Delta\nabla)H_p}. \quad (23)$$

An important question concerns how to interpret and measure the temperature and velocity fluctuations T' and v_c in the simulations for comparison to mixing length theory. In the mixing length theory, these fluctuations are identified with the properties of large eddies. Therefore, a direct comparison would entail isolating the large eddies from the rest of the flow, and measuring their properties. In lieu of this complicated procedure we identify the fluctuations in the large eddies with two distinct quantities for comparison: (1) the r.m.s. fluctuations in the flow; (2) the difference between the horizontally averaged background value and the mean values in the up and down flowing material.

The temperature fluctuations calculated using these two methods are presented in Figure 17. The temperature fluctuations in the convection zone follow a trend similar to the super-adiabatic gradient, i.e., decreasing with increasing radius. In the right panel of Figure 17 the radial profile of α_T is shown using both definitions of the fluctuations. The nonzero temperature fluctuations outside the convective region are due to distortions in stable layers due to convective buoyancy braking Meakin & Arnett (2006b); the use of separate up and down flows is cleaner, eliminating these. The slope in the temperature fluctuation profiles are slightly overcompensated for by the super-adiabatic gradient when forming the ratio α_T . Within the scatter, however, α_T is fairly well represented by a constant value. The mean value within the body of the convection zone (taken to be $r \in [0.5, 0.75] \times 10^9$ cm) is larger for the r.m.s. fluctuations $\langle\alpha_T(\text{rms})\rangle = 0.73$ compared to $\langle\alpha_T(\text{up})\rangle = 0.45$ and $\langle\alpha_T(\text{down})\rangle = 0.40$. The largest departures from the mean, within the convective region, occur at the base of the convection zone, $r \lesssim 0.52 \times 10^9$ cm, where the nuclear flame is driving the convective flow. The departures are also large at the top, in the region of buoyancy braking.

The corresponding analysis for the velocity fluctuations is presented in Figure 18. The overall trends are similar for α_T and α_v . The mean values of α_v

within the body of the convection zone are $\langle\alpha_v(\text{rms})\rangle = 1.22$, $\langle\alpha_v(\text{up})\rangle = 1.08$, and $\langle\alpha_v(\text{down})\rangle = 0.96$. The largest departure from constancy is again found to be at the base of the convection zone (the flame region).

The sharp decrease in the effective mixing length near the lower boundary is not entirely surprising. The distance to the convective boundary provides an upper limit to the mixing length, while further away from the boundaries the mixing length is limited by the distance over which eddies can maintain their coherence. This effect is possibly more exaggerated at the lower boundary because of the steep gradient in velocity which is needed to move the energy out of the burning zone. In contrast, the upper boundary is characterized by a more gentle deceleration of material and a "softer" boundary (i.e., lower N^2). Ignoring this boundary effect and using the same mixing length parameter throughout the convection zone would result in a shallower temperature gradient near the boundary. The stiff temperature dependence of the nuclear reaction rates may therefore be affected.

The absolute calibration of α_T and α_v are somewhat arbitrary, and are scaled by factors of order unity for a particular implementation of the mixing length theory based on the heuristic arguments discussed above. According to equations 15, 16, 22, and 23 the equivalencies are $\alpha_{\Lambda,T} = 2 \times \alpha_T$ and $\alpha_{\Lambda,v} = \sqrt{2} \times \alpha_v$ where the values subscripted by Λ indicate the mixing length theory values defined by Kippenhahn & Weigert (1990). The corresponding values measured in the simulation are $\langle\alpha_{\Lambda,v}(\text{rms})\rangle = 1.73$, $\langle\alpha_{\Lambda,v}(\text{up})\rangle = 1.53$, and $\langle\alpha_{\Lambda,v}(\text{down})\rangle = 1.35$, for velocity fluctuations; and $\langle\alpha_{\Lambda,T}(\text{rms})\rangle = 1.46$, $\langle\alpha_{\Lambda,T}(\text{up})\rangle = 0.9$, and $\langle\alpha_{\Lambda,T}(\text{down})\rangle = 0.8$ for temperature fluctuations.

The ratios $\alpha_{\Lambda,T}/\alpha_{\Lambda,v}$ are 0.84, 0.59, and 0.60 for the r.m.s., up-flow, and down-flow values, respectively. In relation to the present simulation, a higher degree of consistency (i.e., $\alpha_{\Lambda,v} = \alpha_{\Lambda,T}$) can be brought to this implementation of the mixing length theory by scaling the velocity fluctuation in equation 16 by the inverse of the ratio $\alpha_{\Lambda,T}/\alpha_{\Lambda,v}$. Physically, this translates into a higher efficiency (by a factor $\sim 1.2 - 1.7$) for the buoyancy work to accelerate the large eddies over the value of 1/2 adopted above, which is reasonable considering the heuristic argument used. Alternatively, agreement can be made by scaling the temperature fluctuations in equation 15 by the same ratio, which amounts to decreasing the distance over which eddies remain coherent and adiabatic as they move across the convection zone. Both of these effects are plausible, as well as a combination of the two so long as the ratio is maintained. Which is operating in the present simulation? Unfortunately, the degeneracy between these two parameters cannot be broken because they combine linearly when calculating the enthalpy flux, which therefore does not provide a further constraint. Finally, *it is possible that the effective mixing lengths for temperature and velocity fluctuations are different*, a notion that is supported by the correlation lengths which we discuss next.

6.3. Correlation Length Scales

In the top two panels of Figure 19 the vertical correlation length scales, calculated according to equation B1, are presented for the velocity and temperature fluctuations. The vertical scale height is defined as the full

width at half maximum of the correlation function, and can be written in terms of the correlation length in the positive and negative directions, $L_V = L_V^+ - L_V^-$. The relative values of L_V^+ and L_V^- give an indication of asymmetries in the eddies (Figure 19, lower-left): $L_V^+/L_V^- = 1$ is a symmetric eddy; $L_V^+/L_V^- > 1$ is an eddy flattened on the bottom; and $L_V^+/L_V^- < 1$ is an eddy flattened at the top. Based on this simple diagnostic both the temperature and velocity correlations indicate that the eddies near the lower boundary are flattened on the bottom, and those at the upper boundary are flattened on the top. The "overshooting" distance ($h \sim 10^7$ cm at the upper boundary and $h \lesssim 10^6$ cm at the lower boundary), which is best described as an elastic response to the incoming turbulent elements, is very small compared to the correlation lengths measured here. Therefore, these eddies are effectively hitting a "hard wall" upon reaching the boundaries.

The signature of this eddy "flattening" is also present in the radial profile of the full width length scale, L_V . In the case of velocity, which has larger correlation length scales, significant asymmetries are present throughout the convection zone. The smaller length scales associated with the temperature fluctuations permit a broad region throughout the convection zone where the eddies are roughly symmetric ($L_V^+/L_V^- \approx 1$) and appear to be uninfluenced by the boundaries. In this intermediate region, away from the boundaries, the temperature fluctuation length scales are relatively constant in size, even decreasing with radius, in contrast to the pressure and density scale heights which are increasing with radius.

In the standard mixing length theory, the sizes of convective eddies are assumed to be comparable to the size of the mixing length. How do the correlation length scales compare to the mixing length parameters found above? The lower left panel of Figure 19 shows the ratios of L_V to the pressure and density scale heights. None of these curves are particularly constant within the convection zone, and boundary effects are particularly strong throughout the convection zone in the case of the velocity correlations. Interestingly, the velocity correlation parameter $\alpha_v(v_r, H_p) = L_V(v_r)/H_p$ is larger than the temperature correlation parameter $\alpha_v(T', H_p) = L_V(T')/H_p$. This is in accord with the ratio $\alpha_{\Lambda, T}/\alpha_{\Lambda, v} < 1$ found in the mixing length analysis above. Concerning the absolute calibration, however, *the correlation length scales are smaller than the mixing length values by as much as a factor of a few*. In an analogous comparison by Robinson et al. (2004) for subgiant atmosphere models, the vertical correlation lengths were also found to be smaller than the mixing length used to construct the initial model, and that the ratio varied significantly throughout the convection zone.

The horizontal correlation lengths L_H are shown in Figure 20 together with the vertical scales for comparison. For the velocity, the horizontal scale is much smaller than the vertical, indicative of eddies which are significantly elongated in the vertical direction. The temperature fluctuations appear to be much more symmetric, with only a small degree of elongation in the vertical direction which is slightly more pronounced near the top of the convection zone. In the stable layers, the horizontal scales are larger than the vertical, which is a characteris-

tic of the horizontal "sloshing" motions associated with g-modes.

6.4. The Kinetic Energy Flux, Flow Asymmetry, and Moving Beyond the Mixing Length Theory

The kinetic energy flux associated with convection is ignored in the mixing length theory since it arises from the *asymmetries* in the flow and MLT assumes that the flow is symmetric. An order of magnitude estimate for the kinetic energy flux, however, can be made:

$$\frac{F_K}{F_c} \sim \frac{\rho v_c^2/2}{\rho c_p T' v_c} \sim \frac{\alpha_\Lambda}{8} \frac{\beta P}{T \rho c_p} = \frac{\alpha_\Lambda}{8} \nabla_{ad} \sim 0.03 \quad (24)$$

where mixing length relationships have been used to calculate v_c and T' , α_Λ is assumed to be of order unity, and $\nabla_{ad} \sim 0.25$ has been adopted from the simulation. This result tells us that the kinetic energy flux will be a few percent of the convective enthalpy flux. This estimate is an upper limit since up-flows and down-flows will cancel to some degree (Böhm-Vitense 1992, §6.1). In the simulation, the ratio of kinetic to enthalpy flux is found to be $F_{K,max}/F_{c,max} \sim 0.01$, which is of order the simple MLT scaling, but down by a factor of a few as expected.

We can directly relate the kinetic energy flux to the flow asymmetry in the following way. The upflow area covering fraction $f_u = A_{up}/A_{tot}$ is shown in Figure 21. We can then write an estimate for the kinetic energy flux as,

$$F_{K,net} = \frac{1}{2} \rho_0 (f_u v_u^3 - f_d v_d^3) \quad (25)$$

which can be written in terms of just the flow velocities,

$$F_{K,net} = \frac{1}{2} \rho_0 \left[\frac{v_u^3 + v_d^3}{v_u/v_d + 1} - v_d^3 \right] \quad (26)$$

where we have used the mass conservation equation, $f_u v_u + f_d v_d = 0$ assuming $\rho_u \approx \rho_d$ which is a good approximation in these simulations. The kinetic energy flux in the simulation is shown in Figure 22. Shown by the thin line is F_K calculated according to equation 26, which is in good agreement. Here, we have used the horizontal and time averaged values for $\langle v \rangle$ and $\langle v^3 \rangle$. The mixing length theory, however, does not provide information about $\langle v^3 \rangle$, but only $\langle v \rangle$. We overplot with the dashed line F_K calculated using $\langle v \rangle^3$ in place of $\langle v^3 \rangle$; it has to be scaled by a factor of 5 to fit the simulation data.

The scaling factor needed to calculate the kinetic energy flux is required to account for the skewness in the radial velocity field. More precisely, the correlation coefficient $\chi = \frac{\overline{\langle v_u^3 \rangle} / \overline{\langle v_u \rangle^3}}{\overline{\langle v_u^3 \rangle} / \overline{\langle v_u \rangle^3}}$ is needed, which is related to the skewness $\gamma = \frac{\overline{\langle v^3 \rangle} / \sigma_v^3}{\overline{\langle v^3 \rangle} / \sigma_v^3}$. Both χ and γ are presented in Figure 22. Note, that the skewness is a good proxy for the down-flow covering fraction ($f_d = 1 - f_u$; see Figure 21), and therefore its sign is indicative of the direction of the kinetic energy flux.

Convective regions which are spanned by several pressure scale heights are found to have kinetic energy to enthalpy flux ratios larger than a few percent as found in this study. For instance, the simulations of Cattaneo et al. (1991) and Chan & Sofia (1989) which each span ~ 5

pressure scale heights achieve $|F_K/F_c| \sim 35\%$, and the domain in Chan & Sofia (1996) spanning ~ 7 pressure scale heights achieves $|F_K/F_c| \sim 50\%$. A key result in the analysis of Cattaneo et al. (1991) is that the kinetic energy flux is dominated by coherent, downward-directed flows which are correlated over distances comparable to the simulation domain. Additionally, the enthalpy flux and kinetic energy fluxes associated with these downflows essentially cancel with $c_p T' \sim v_c^2$, which was shown to follow if the downflows can be described as Bernoulli streamlines.

The long range correlations just described, together with the boundary effects which dominate our shell burning model, undermine the basic mixing length theory picture of convection. The large coherence of the flows seen in these simulations, however, and present even in turbulent parameter regimes, suggest that modeling these *coherent structures* is a viable approach. Already, models incorporating multiple streams or "plumes" as closure models (e.g. Rempel 2004; Lesaffre et al. 2005; Belkacem et al. 2006) are providing enticing alternatives to the mixing length theory.

6.5. Related Studies

Although the mixing length parameters calculated above deviate from constancy near the convective boundaries, a mean value is a good approximation for most of the convection zone. It would be interesting if these parameters α_E , α_T , and α_v were universal, as assumed by mixing-length theory. If we restrict consideration to 3D compressible convection simulations for simplicity and homogeneity, there are several previous studies which have confronted mixing length theory to which we can compare our results. These studies investigate convection under diverse conditions, including slab convection (Chan & Sofia 1987, 1989, 1996; Porter & Woodward 2000), a red giant envelope (Porter, Woodward, & Jacobs 2000), and solar and sub-giant surface layers (Kim et al. 1995, 1996; Robinson et al. 2003, 2004, 2005). The number of zones used range from 1.9×10^4 (Chan & Sofia 1989) to 6.7×10^7 (Porter & Woodward 2000). The equations of state used include a gamma-law (Chan & Sofia 1989; Porter & Woodward 2000), ionized gas (Kim et al. 1996; Robinson et al. 2004), and a combined relativistic electron plus ion gas (Timmes & Swesty 2000) in this paper. Subgrid scale physics was treated by a Smagorinsky model (Smagorinsky 1963) or by ignoring it. We note that Styne, et al. (2000) have shown that PPM methods solving the Euler equations converge to the same limit as solutions to the Navier-Stokes equations, as resolution is increased and viscosity reduced. Additionally, the subgrid scale turbulence "model" implicit in the numerical algorithm of PPM is known to be well behaved (Fernando Grinstein, personal communication). Given this already inhomogeneous set of simulations, determining consistent convection parameters is difficult. Our attempt is given in Table 4, in which we summarize the convection parameters found in these studies for comparison to our own.

How well do these compare? In some respects the agreement is striking. The parameter α_E is in the range $\sim 0.7 - 0.8$ for all groups. Further, all agree that for their case, the mixing-length theory gives a fairly reasonable representation of the simulations in the sense that the

alphas are roughly constant throughout the body of the convection zone. The difficulty is that the specific values of these alphas depend upon the case considered. The two best-resolved simulations, ours and (Porter & Woodward 2000), use the same solution method, PPM, yet have the most differing alphas. This suggests to us that the differences are due to the physical parameters of the respective convection zones. Porter, Woodward, & Jacobs (2000) have already shown that slab and spherical geometry give qualitatively different behavior for the alphas. Our shell is only two pressure scale heights in depth, and is relatively slab-like; Porter & Woodward (2000) have a convection zone which is more than twice as deep by this measure. There is a suggestion in Table 4 that the alphas increase with the depth of the convection zone. This would be reasonable if a convective plume were accelerated through the whole convection region before it is decelerated at the nonconvective boundary. However, the other differences mentioned above probably contribute to the scatter in the alpha parameters in 4.

Further efforts on this issue are needed. If convection does depend upon the nonlocal, physical structure of the star, calibration of the mixing length to fit the sun, as is traditionally done, is not wise. Furthermore, it is well known that the mixing length theory is particularly prone to problems in the surface layers where convection becomes inefficient. Therefore, the empirical agreement of mixing length calibration to the sun and to Population II giants (Ferraro, et al. 2006) may be a fortuitous coincidence.

7. MIXING AT CONVECTIVE BOUNDARIES

The boundaries which separate the convective regions from the stably stratified layers in our 3D simulations span a range of relative stability, with $1 \lesssim Ri_B \lesssim 420$. At the lowest values of Ri_B , the boundary is quickly overwhelmed by turbulence, as described in §4.1. Once Ri_B becomes large enough, the boundary becomes stabilizing and evolves over a much longer timescale. Snapshots of the quasi-steady shell burning and the core convection boundaries are presented in Figure 23, ordered by Ri_B with spans the range $36 \lesssim Ri_B \lesssim 420$. The anatomy of the convective interfaces includes the turbulent convection zone, the distorted boundary layer of thickness h , and the stably stratified layer with internal wave motions (compare to Figure 1).

The boundary becomes more resilient to thickening, and distortion by the turbulence as Ri_B increases. A region of partial mixing exists primarily on the turbulent side of the interface, where material is being drawn into the convection zone. The "ballistic" picture of penetrative overshooting (Zahn 1991) in which convective eddies are envisioned to pierce the stable layer does not obtain. Instead, material mixing proceeds through instabilities at the interface, including shear instabilities and "wave breaking" events, which break the boundary up into wisps of material that are then drawn into the turbulent region and mixed. The convective interface remains fairly sharp in all cases, and the effective width is well described by the elastic response of the boundary layer to incoming eddies, $h \sim v_c/N$. The convective interfaces seen in our simulations bear a striking resemblance to those observed in laboratory studies of turbu-

lent entrainment of comparable Ri_B (see e.g. McGrath et al. 1997, Figs. 2-5).

The mixing that occurs due to the instabilities and eddy scouring events at the interface leads to a steady increase in the size of the convection zone. In this section we quantify the entrainment rates at the convective boundaries, we discuss these results in terms of the buoyancy evolution of the interface, and we describe how the "turbulent entrainment" process can be incorporated into a stellar evolution code as a dynamic boundary condition to be used in addition to the traditional static Ledoux and Schwarzschild criteria. We conclude the section with some comments on numerical resolution.

7.1. Quantifying the Boundary Layer Mixing Rates

As evident in Figure 23, the convective boundary layers are significantly distorted from spherical shells. To estimate the radial location of the interface we first map out its shape in angle $r_i = r_i(\theta, \phi)$. At each angular position the surface is taken to be coincident with the radial position where the composition gradient is the steepest (this is comparable to the location of minimum density scale height $H_\rho = [\partial \ln \rho / \partial r]^{-1}$). The interface thickness h is taken to be the r.m.s. variation of the surface r_i with angle, $h = \sigma[r_i(\theta, \phi)]$, which provides a quantitative measure of the amplitudes of the distortions imparted to the interface. The mass interior to the interface is calculated according to,

$$M_i = \int_{r_0}^{\langle r_i \rangle} 4\pi r^2 \langle \rho \rangle dr \quad (27)$$

where r_0 is the inner boundary of the computational domain, $\langle \rho \rangle$ is the horizontally averaged density, and the mean interface radius is used for the upper limit on the integral. The time derivative \dot{M}_i is the rate at which mass is entrained into the convection zone.

In Figure 24 the time histories of the averaged interface location $\langle r_i \rangle$ and interfacial thickness h are shown for the convective boundaries in our simulations. A 3D model and a representative 2D model are shown for each boundary. The outer shell boundary layer adjusts rapidly in the first 100s to a new position, due to the penetration event discussed in §4.1, after which a slow outward migration ensues. For the 3D model, the outward migration proceeds in distinct stages, labeled (a - c) in Figure 24. Each stage is well described by a linear increase of radius with time, and ends with a rapid adjustment to a new entrainment rate. This behavior can also be seen in Figure 4, where the change in entrainment rate is coincident with changes in the background composition gradient and stability (compare to the initial buoyancy frequency profile in Figure 2).

The downward migration of the lower shell boundary is more uniform and proceeds at a significantly reduced rate compared to the upper boundary. The core convection boundary evolution departs most significantly from a linear trend, but Monotonic growth is clearly established very soon after the simulation begins $t \gtrsim 2 \times 10^5$ s.

The interfacial thickness h in the oxygen burning models are initially large, reflecting the strong mixing event during the initial transient, but settle down to relatively constant values for $t \gtrsim 300$ s. In contrast, the boundary

thickness in the core convection model increases gradually with time until a steady state value is achieved, reflecting the milder initial development. In all cases, the time averaged values of h during the quasi-steady states compare well to the boundary displacement expected for eddies impacting the stable layer with the characteristic convective velocities of the model, $h \sim v_c/N$.

The entrainment rate and the interfacial thickness is larger in all of the 2D models as a consequence of the larger velocity scales in those simulations. The interface migration rates and averaged interfacial layer thicknesses are tabulated for all of the models in Tables 5 and 6, and are broken down into various time intervals over which linear growth of the boundary is a good approximation. Time averaged mass entrainment rates are also included in Tables 2 and 3.

7.2. The Entrainment Energetics

In order for entrainment to take place at a convective boundary the buoyancy increment of the stable layer material over that of the mixed layer material must be overcome. This can happen in two distinct ways. First, non-adiabatic processes can change the relative stability of the stable layer. For example, heating the convective region will cause an increase in its entropy, and the buoyancy jump separating the overlying layer will decrease. The rate at which the convective boundary will grow due to heating is $u_s = \dot{s}/(\partial_r s)$, where $\partial_r s$ is the radial gradient of entropy at the boundary and \dot{s} is the time rate of change of entropy in the shell. This process will cause both the upper and lower boundaries to migrate to larger radii – the upper boundary will be weakened, while the lower boundary will become stiffer. Non-adiabatic processes in the boundary layers will affect their stability in the same way: cooling in the upper and heating in the lower boundaries will weaken their stratification.

A related, but distinct process is "turbulent entrainment" whereby turbulent kinetic energy does work against gravity to draw material into the turbulent region. In this process, the stratification is weakened at a convective boundary by the turbulent velocity fluctuations. This is quantified in terms of the buoyancy flux $q = g\rho'v'/\rho_0$. In the absence of heating and cooling sources the buoyancy in the interfacial layers will evolve according to the buoyancy conservation equation,

$$\partial_t b = -\text{div}(q) \quad (28)$$

and a positive flux divergence at the boundary will lead to a weakening of the stratification. The relationship between turbulent entrainment and the weakening of a boundary through heating and cooling can be understood in terms of the enthalpy flux which attends the buoyancy flux. In fact, the buoyancy flux is directly related to the enthalpy flux across the interface,

$$F_c = \rho_0 c_p \langle T' v_r' \rangle = \frac{c_p T_0}{\beta} \langle \rho' v_r' \rangle = \rho_0 c_p \frac{T_0}{\beta g} \times q \quad (29)$$

and is equivalent to heating and cooling processes operating in the boundary layer (note the downward directed enthalpy flux within the boundary layers in Figure 15).

What drives the entrainment seen in the present simulations? Can the entrainment in the outer shell boundary be explained by the heating of the convection zone

by nuclear burning? Comparing the entropy growth rate of the shell to the entropy gradient at the boundary we find $u_s \sim 0.8 \times 10^4$ cm/s, which is at most 17% of the measured growth rate for this boundary, and typically of order a few percent. Shell heating will reduce the growth rate of the lower boundary by $u_s \sim 0.04 \times 10^4$ cm/s, which is of order a few percent of the rate measured. Therefore, the overall heating and cooling of the shell contributes very modestly to the growth of the shell over the course of the simulation. The long thermal timescale in the core convection model reduces this effect even more, where it is lower by several orders of magnitude. Therefore, we turn to the turbulent hydrodynamic processes operating in the boundary layer to understand the growth of the convection zones.

In Figure 25 we present the buoyancy flux profiles for our 3D simulation models, including both time-series diagrams and time averaged radial profiles. The properties of the buoyancy flux can be divided into three distinct flow regimes: (1) the body of the buoyant convecting layer, which is dominated by positive q ; (2) the convective boundary layers, with negative q ; (3) the stably stratified layers, where q is oscillatory, but has a nearly zero mean (in both a horizontal and time average sense).

The buoyancy driving of the convective flow in regime (1) can be appreciated by comparing the flow velocity to the commonly used buoyant convection velocity scale $v_*^3 = 2.5 \int \langle q \rangle dr$, where integration is taken over the radial extent of the convection zone (see e.g. Deardorff 1980). v_* for the 3D shell burning and core convection models are $v_* \sim 10^7$ cm/s and $v_* \sim 3 \times 10^5$ cm/s, which compare well to the radial r.m.s. turbulent velocities measured in the simulation (Figures 6 and 12).

In regime (2), which occurs in the convective boundaries, the buoyancy flux is negative. A negative value of q signifies that the turbulent kinetic energy is being converted into potential energy. The mixing that attends this negative buoyancy flux underlies the entrainment that is taking place at the boundaries through equation 28. We demonstrate this by showing that the entrainment speeds measured in the simulation are consistent with the measured buoyancy fluxes. The interface migration speed is incorporated into the conservation equation by writing the time derivative as an advective derivative,

$$\partial_t b \sim u_e \partial_r b = u_e N^2 \quad (30)$$

where we have used the relationship $\partial_r b = N^2$. Using this time derivative in equation 28 and solving for u_e we find,

$$\tilde{u}_e = \frac{\Delta q}{h N^2} \quad (31)$$

where we have approximated the divergence of the buoyancy flux with the difference $\Delta q/h$. We use the symbol \tilde{u}_e to distinguish the estimated rate from the values measured in the simulation.

If we adopt the buoyancy flux at the interface for Δq (Figure 25), the measured interface thickness h , and the buoyancy frequency at the boundary, we find the following entrainment rates. For the upper shell boundary, lower shell boundary, and the core convection boundary we have: $\tilde{u}_e \sim 5.1 \times 10^4$ cm/s; $\tilde{u}_e \sim 1.1 \times 10^4$ cm/s; and $\tilde{u}_e \sim 2.2 \times 10^3$ cm/s, respectively. These are to be

compared with $u_e = |r_i - v_{exp}|$ measured in section §7.1 and presented in Tables 5 and 6. The values corresponding to the same time period are: $u_e = 4.6 \times 10^4$ cm/s; $u_e = 1.2 \times 10^4$ cm/s; and $u_e = 2 \times 10^3$ cm/s. Although these estimates are only order of magnitude (e.g., using the crude approximation for the time derivative in eq. [30]) they compare well to the values measured in the simulations and the buoyancy flux due to "turbulent entrainment" can account for the growth of the convective layers seen here.

7.3. Whence q ?

The buoyancy flux q appears as a term in the turbulent kinetic energy (TKE) equation, which we present in §A (eq. [A12]). In our notation, the buoyancy flux is related to the buoyancy work term by $q = \langle W_B \rangle / \rho_0$. The buoyancy flux, therefore, is related to the rate at which turbulent kinetic energy is advected into the stable layer F_K , the rate at which it dissipates through viscous forces ε_K , and the rate at which energy is transported through the boundary layer by pressure-velocity correlations F_p . In essence, entrainment is the process by which the turbulent kinetic energy in the boundary layer does work against gravity to increase the potential energy of the overall stratification.

Two theoretical approaches have been taken to study entrainment. The first approach ignores the TKE equation and instead posits an "entrainment law". The entrainment law is merely a functional form for the rate at which stable layer mass will flow into the turbulent region, and is therefore a dynamic boundary condition. These laws are usually parameterized by the stability properties of the interface and the strength of the turbulence through Ri_B (see e.g. Fedorovich, Conzemius & Mironov 2004). Once an entrainment law is adopted, the enthalpy flux can be calculated and the evolution of the boundary can be self-consistently solved for. The advantage of such an entrainment law is the simplicity with which it can be incorporated into global circulation models of the atmosphere, for instance.

An alternative approach to adopting an entrainment law is an explicit physical model for the terms in the TKE equation (eq. [A12]). For example, general forms for the buoyancy flux profile within the stable layer have been applied with some success in reproducing the growth of the atmospheric boundary layer and the deepening of the oceanic thermocline (Stull 1976b; Deardorff 1979; Fedorovich & Mironov 1995). In some respects, however, these models are glorified entrainment laws since the buoyancy flux is prescribed in a simplified, parameterized way. Moving beyond assumptions concerning the turbulence profiles within the interfacial layer, are theoretical models which take into account the interactions of waves and turbulence and incorporate non-linear models for the evolution of instabilities (e.g. Carruthers & Hunt 1986; Fernando & Hunt 1997). The approach adopted in these theoretical studies is general enough that any adjustable parameters may turn out to be universal and a predictive model can be developed. In addition, the framework employed is general enough that the production of turbulence by mean flows (i.e., stellar rotation) can be incorporated, as well as long-range effects due to internal waves. The internal waves are incorporated through the pressure-correlation flux, F_p , and plays a

central role in the evolution of the buoyancy flux when wave breaking is important.

7.4. An "Empirical" Entrainment Law

The development of a sophisticated turbulence model to explain entrainment is beyond the scope of the present work. Instead, we ask to what extent do the entrainment laws used in geophysical models apply to our simulations and stellar interiors? Guided by laboratory study and geophysical large eddy simulation we study the dependence of the entrainment rate on the bulk Richardson number.

Ri_B is calculated according to equation 1, where we use the horizontal correlation length scale $L = \mathcal{L}_H$ defined in §B. The buoyancy jump is calculated by performing the integration in equation 2 over the width of the interface which we take to be the interval $r \in [\bar{r}_i - h, \bar{r}_i + h]$. The normalized entrainment rates $E = u_e/\sigma$, the buoyancy jumps Δb , and Ri_B are presented in Tables 5 and 6. The dependence of the entrainment coefficient E on Ri_B is presented in Figure 26.

The 2D and 3D data are found to obey similar trends (lower E for higher Ri_B), but occupy significantly different regions of the diagram. This can be explained by the much higher r.m.s. velocities in the 2D simulation. The velocity scale in 2D is apparently an artifact of the reduced dimensionality of the problem which significantly influences the flow morphology. Although the velocity scale is higher in the 2D models, it is much more laminar and accompanied by less turbulent mixing. The arrow in Figure 26 indicates the direction that the 2D data points would move if a lower effective r.m.s. velocity were assumed. In what follows we focus our attention exclusively on the entrainment data found for the more realistic 3D models.

What we find is that the entrainment coefficient E is well described by a power law dependence on Ri_B of the form in equation 4. Our best fit values for the parameters are $\log A = 0.027 \pm 0.38$ and $n = 1.05 \pm 0.21$. This entrainment law is shown by a dashed line in Figure 26. Remarkably, the power law is of order unity, in agreement with geophysical and laboratory studies. The fact that the entrainment in our simulations are governed by the same, fairly universal dependence on Ri_B as these other studies may have been anticipated, considering the striking degree of similarity between the buoyancy profiles and the character of the developed flow in the vicinity of the boundary (Figure 23).

7.5. A Dynamic Convection Zone Boundary Condition

Mass entrainment is a fundamentally different phenomena from diffusion, which is the typical route used to incorporate new mixing phenomena into a stellar evolution code. Therefore, how might we incorporate this new process? Schematically, the idea is very simple. For each convective boundary, initially found with the traditional stability criteria ($\partial s/\partial r = 0$, $\partial^2 s/\partial r^2 \neq 0$), we can calculate the associated bulk Richardson number based on the background stratification and an approximation of the turbulence characteristics (e.g., from MLT). With Ri_B in hand we can then input this into our entrainment law, $E = E(Ri_B)$ which returns to us the entrainment rate. The entrainment rate, therefore, is the boundary

growth rate as a function of Ri_B and possibly other parameters of the system. The function $E(Ri_B)$ can be broken up into at least three regimes for convenience.

Low stability: $Ri_B < Ri_B^{min}$. For low Ri_B it is observed that mass entrainment happens very quickly, on an advection timescale (§4.1). Therefore, we can define a minimum Ri_B^{min} at which the expansion of the convection zone will proceed very quickly, eliminating convective boundaries which are too weak to support the adjacent turbulence.

Intermediate Stability: $Ri_B^{min} < Ri_B < Ri_B^{max}$. For an intermediate range of stability, we can use the fairly universal entrainment law which matches our simulation data, defined by the two parameters A and n . Although scatter in mixing rates were found to be as large as a factor of a few relative to the best fit law, the general monotonic, power-law dependence was found to be robust. We can incorporate this physics into the stellar evolution code as a mass entrainment rate,

$$\dot{M}_E = \frac{\partial M}{\partial r} u_E = (4\pi r_i^2 \rho_i) \sigma_H \times f_A \times 10^{(-n \log Ri_B)} \quad (32)$$

where the normalization factor is written $f_A = 10^{(\log A)}$ and represents the turbulent entrainment mixing efficiency. More sophistication can subsequently be incorporated as our understanding of the entrainment process improves.

High Stability: $Ri_B > Ri_B^{max}$. The entrainment process will cease to operate at some upper limit Ri_B^{max} , above which the boundary evolution will be controlled by diffusive processes on the molecular scale. Following (Phillips 1966), we have,

$$Ri_B^{max} \simeq \left(\frac{u_E}{\sigma}\right) \left(\frac{\sigma L}{\kappa}\right) \quad (33)$$

which is based on the condition that the kinetic energy in the turbulence is sufficient to lift the material from the interface, $\rho \sigma^2 \gtrsim \rho N^2 \Delta^2$. Here, the interface thickness is taken to be that due to molecular diffusion with $\Delta \gtrsim \kappa/u_E$. The relatively small diffusion rates in stellar interiors imply that turbulent entrainment will continue to operate to very high Richardson numbers. For comparison, the entrainment process in the ocean is estimated to operate up to $Ri_B \sim 10^{5-6}$.

Additional details concerning the implementation of this type of boundary condition into TYCHO will be presented in a subsequent paper.

7.6. Spatial Scales, Numerical Resolution, and Entrainment

We conclude this section with a few comments on how well simulation can be trusted in elucidating the process of entrainment, which is not very well understood. The spatial scales which limit the entrainment rate at a convective boundary are not also not well understood, and depend on the interplay between large eddy and small scale turbulent transport processes. As discussed by Lewellen & Lewellen (1998), there is feedback between the transport rate away from the turbulent boundary layer which is controlled by large eddies, and the transport rate of material in the immediate vicinity of the interface by small scale turbulence. A full understanding

of this problem hinges on being able to resolve the entrainment zone in the presence of the large scale eddies.

A code comparison and resolution study of the entrainment problem in the planetary boundary layer context was conducted by Bretherton et al. (1999) and Stevens & Bretherton (1999). In these studies, it was suggested that the appropriate criteria for resolving boundary layer entrainment is that the grid zoning is smaller than the fluctuations induced in the inversion layer by the large eddies so that shear instabilities (e.g., Kelvin-Helmholtz) would not be suppressed. It was suggested that a "nested grid" of refinement within the boundary layer was comparable to using fine resolution throughout the simulation domain. The suggested resolution criterion in these papers, however, fail to account for the non-linear turbulent evolution which proceeds the onset of instabilities. In addition, no simulations were conducted with enough resolution that the boundary layers were turbulent, and the simulations presented were even marginally resolved by the author's suggested criteria.

A related study by Alexakis (2004) investigates the entrainment and mixing at a boundary due to internal gravity wave breaking driven by a shear flow. This process may be operating in the shear mixing layers that form when large eddies impact the boundary layer. In this study, the mass entrainment rate was found to depend on the numerical resolution in a non-monotonic way, first decreasing and then increasing with finer resolution. The author concludes that low resolution models are dominated by numerical diffusion until the resolution is fine enough to resolve turbulence near the boundary, at which point the entrainment rate begins to increase and is controlled by turbulent transport. Although the asymptotic mixing rate was inconclusive and no resolution criteria was proposed, resolving the turbulence ensuing from the instability was shown to be important.

Much more work needs to be done to address the role played by both the small scale processes and the interplay with large eddies. Two complimentary numerical approaches can be taken. First, the feedback between large and small scale mixing and transport processes can be studied using large eddy simulation with a range of subgrid scale mixing efficiencies. Such a study can help develop insight into which scales control the mixing rate. Second, direct numerical simulations (DNS) which resolve the turbulent processes operating at the interface can be undertaken when sufficient computational resources are available. These studies would provide more definitive conclusions concerning the interplay between eddy scales and would provide guidance for a more general framework for future theoretical analysis. Finally, it is important to keep in mind that laboratory studies of high Reynolds number turbulent entrainment continue to provide useful constraints, and improved flow visualization techniques are allowing a more direct comparison to theory and simulation.

The "empirical" entrainment law which we discuss in this paper is constrained by only a few data points (the six 3D data points in Figure 26). Extending simulations to include an ever more diverse suite of stellar structures would provide an even stronger mandate, and better constrained model for incorporating this physics into stellar evolution codes.

8. SUMMARY AND CONCLUSIONS

In this paper, we have presented the results of three-dimensional, reactive, compressible, hydrodynamic simulations of deep, efficient stellar convection zones in massive stars. Our models are unique in terms of the degree to which non-idealized physics have been used, and the evolutionary stages simulated, with fuel and ash clearly distinguished.

We find several general results regarding the basic properties of the convective flow:

- the flow is highly intermittent, but has robust statistical properties,
- the 2D vs 3D velocity scales differ by almost a factor of several, and the flow morphologies are completely different,
- stable layers interact with convection to decelerate plumes, and consequently distort these layers, which then generate waves,
- mixing is found to occur at convective boundaries in manner best described as turbulent entrainment, rather than the traditional picture of convective overshooting wherein turbulent eddies ballistically penetrate the stable layers.

We have compared our oxygen shell burning model to mixing length theory assumptions. We show that, while a reasonable representation of the super-adiabatic temperature gradient and velocity scale can be fit with a single mixing length, the values of the inferred mixing-length "constants" differ from other simulations. This was already implied in Porter, Woodward, & Jacobs (2000), who found difference for slab and spherical geometries. There may be a dependence upon the depth of the convection zone as well, and possibly upon the nature of the stable boundary regions and/or the nature of the driving process (burning or radiative loss).

Why do we care about MLT in regions of efficient convection? (1) temperature profile can affect the burning rates, which have a stiff temperature dependence; (2) the velocity scale can affect the nucleosynthesis (such as s-process branching ratios in double shell burning AGB stars) by dictating the exposure time of the plasma to varying conditions throughout the burning region; (3) the velocity scale and the kinetic energy flux is an important input needed for calculating the mixing at convective boundaries.

We have found that the extent of mixing is better represented by an integrated Richardson number rather than the convective Schwarzschild or Ledoux criteria alone. This incorporates the addition physics related to the resistance of stiff boundaries to mixing. Related to the definition of boundary stiffness, we have identified an important physical process which is missing from the standard theory of stellar evolution: turbulent entrainment. This process is well known in the meteorology and oceanographic communities, and has been extensively studied experimentally. We show that the rate of entrainment is well represented as a simple function of the buoyancy jump, in a manner similar to that determined experimentally.

The long term consequences of convective boundary inconsistencies such as the one illustrated by the initial transient in our simulation, and for which the conditions are common in 1D stellar models, can significantly alter the size of convective cores, and thus the subsequent explosion and nucleosynthetic yields of the resultant supernova. In a subsequent paper in this series, we will present case studies which incorporate the physical insight gained through these simulations into the TYCHO stellar evolution code. We expect to see effects in solar models, s-processing in AGB stars, stellar core formation

(white dwarfs, neutron stars, and black holes), stellar nucleosynthesis yields, stellar ages, and HR diagrams.

This work was supported in part by the ASCII FLASH center at the University of Chicago. CM would like to acknowledge the stimulating discussions at the 2006 Los Alamos *Summer Hydro Days* Workshop, made possible by Falk Herwig, which influenced the writing of this paper. DA wishes to thank the Aspen Center for Physics for their hospitality.

APPENDIX

THE ENERGY EQUATION

Total Energy

The primitive energy equation solved by PROMPI is,

$$\partial_t(\rho E) + \nabla \cdot [(\rho E + p)\mathbf{u} + \mathbf{F}_r] = \rho \mathbf{u} \cdot \mathbf{g} + \rho \epsilon_{net} \quad (\text{A1})$$

where the total energy is composed of the internal and kinetic components, $E = E_I + E_K$. We decompose the velocity, density, and pressure fields into mean and fluctuating components according to,

$$\varphi = \varphi_0 + \varphi' \quad (\text{A2})$$

where $\langle \varphi \rangle = \varphi_0$ and $\langle \varphi' \rangle = 0$. The pressure-velocity correlation term is,

$$\nabla \cdot \overline{\langle \rho \mathbf{u} \rangle} = \nabla \cdot \overline{\langle \rho_0 \mathbf{u}_0 \rangle} + \nabla \cdot \overline{\langle p_0 \mathbf{u}' \rangle} + \nabla \cdot \overline{\langle \rho' \mathbf{u}_0 \rangle} + \nabla \cdot \overline{\langle p' \mathbf{u}' \rangle}. \quad (\text{A3})$$

The gravity term is,

$$\overline{\langle \rho \mathbf{g} \cdot \mathbf{u} \rangle} = \overline{\langle \rho_0 \mathbf{u}_0 \mathbf{g} \rangle} + \overline{\langle \rho_0 \mathbf{u}' \mathbf{g} \rangle} + \overline{\langle \rho' \mathbf{u}_0 \mathbf{g} \rangle} + \overline{\langle \rho' \mathbf{u}' \mathbf{g} \rangle}. \quad (\text{A4})$$

The averaging operator eliminates terms which are first order in fluctuations (by definition) and we have,

$$\partial_t \overline{\langle \rho E \rangle} + \nabla \cdot [\overline{\langle \rho E \mathbf{u}_0 \rangle} + \overline{\langle \rho E \mathbf{u}' \rangle} + \overline{\langle p_0 \mathbf{u}_0 \rangle} + \overline{\langle p' \mathbf{u}' \rangle} + \mathbf{F}_r] = \overline{\langle \rho_0 \mathbf{u}_0 \mathbf{g} \rangle} + \overline{\langle \rho' \mathbf{u}' \mathbf{g} \rangle} + \overline{\langle \rho \epsilon_{net} \rangle}. \quad (\text{A5})$$

We can further simplify this expression using the condition of hydrostatic equilibrium, which holds to a high degree of accuracy in the simulation ($\nabla p_0 = \rho_0 \mathbf{g}$). The background velocity in this case, \mathbf{u}_0 , is a slow, highly subsonic, expansion or contraction that is driven on a thermal timescale. The background velocity field has only a radial component (i.e., there is no rotation in the current model), $\mathbf{u}_0 = (u_{0,(r)}, 0, 0)$. The energy equation can be then simplified to read,

$$\partial_t \overline{\langle \rho E \rangle} + \nabla \cdot \overline{\langle \rho E \mathbf{u}_0 \rangle} = -\nabla \cdot \overline{\langle \mathbf{F}_p + \mathbf{F}_I + \mathbf{F}_K + \mathbf{F}_r \rangle} - \overline{\langle p_0 \nabla \cdot \mathbf{u}_0 \rangle} + \overline{\langle \mathbf{W}_b \rangle} + \overline{\langle \rho \epsilon_{net} \rangle}. \quad (\text{A6})$$

where we have used the following definitions,

$$\mathbf{F}_I = \rho E_I \mathbf{u}' \quad (\text{A7})$$

$$\mathbf{F}_K = \rho E_K \mathbf{u}' \quad (\text{A8})$$

$$\mathbf{F}_p = p' \mathbf{u}' \quad (\text{A9})$$

$$\mathbf{W}_b = \rho' \mathbf{g} \cdot \mathbf{u}'. \quad (\text{A10})$$

Kinetic Energy

The kinetic energy equation is derived by forming the scalar product of the velocity with the equation of motion (e.g., Shu, 1992, Ch.2). The momentum equation can be written in vector form as,

$$\partial_t(\rho E_K) + \nabla \cdot (\rho E_K \mathbf{u}) = -\mathbf{u} \cdot \nabla p + \rho \mathbf{u} \cdot \mathbf{g} \quad (\text{A11})$$

Again, we decompose the fields into mean and fluctuating components, employ the hydrostatic equilibrium condition, and perform averages. The result is,

$$\partial_t \overline{\langle \rho E_K \rangle} + \nabla \cdot \overline{\langle \rho E_K \mathbf{u}_0 \rangle} = -\nabla \cdot \overline{\langle \mathbf{F}_p + \mathbf{F}_K \rangle} + \overline{\langle p' \nabla \cdot \mathbf{u}' \rangle} + \overline{\langle \mathbf{W}_b \rangle} - \epsilon_K. \quad (\text{A12})$$

Here, ϵ_K is the viscous dissipation of kinetic energy. In our simulations, this term is not modeled explicitly and arises due to numerical dissipation. The term $p' \nabla \cdot \mathbf{u}'$ represents the compressional work done by turbulent fluctuations, and the other terms are as defined above.

CORRELATION LENGTH SCALES

The vertical correlation of the horizontal distribution of fluctuations in a quantity $X' = X - \langle X \rangle$ at radial position r and offset position $r + \delta r$ is calculated according to,

$$C^V(\delta r; r) = \frac{1}{\Delta\Omega} \frac{\int X'(r, \theta, \phi) X'(r + \delta r, \theta, \phi) d\Omega}{\sigma_X(r) \sigma_X(r + \delta r)} \quad (\text{B1})$$

where the integral is taken over the angular direction with $d\Omega = \sin(\theta) d\theta d\phi$. The correlation is normalized by the product of the horizontal r.m.s. value of the quantity at the two levels being compared σ_X .

The horizontal correlation of fluctuations at radial position r is calculated using the autocorrelation function,

$$C^H(\delta s; r) = \frac{\langle X'(r, s) X'(r, s + \delta s) \rangle}{\sigma_X(r)^2} \quad (\text{B2})$$

where the brackets $\langle \cdot \rangle$ denote averaging over all horizontal locations s and fixed offset δs . The horizontal correlation is normalized by the variance of the quantity σ_X^2 .

Characteristic length scales are defined as the offset position where the correlation function drops to a value of 0.5. For horizontal correlations, we define this length as \mathcal{L}_H . We also define a value which is twice this length, the full width at half maximum, which we denote by L_H . (The value \mathcal{L}_H provides a good approximation to the integral scale, $\int C^H(\delta s; r) d\delta s$.)

In the vertical direction the sign of the offset δr is retained and a separate length scale is defined where the correlation function drops to 0.5 for positive and negative offsets, which we denote by L_V^+ and L_V^- . The full width is denoted $L_V = L_V^+ - L_V^-$.

REFERENCES

- Alexakis, A. 2004, Ph.D. Thesis, U.Chicago
 Alexander, D. R., & Ferguson, J. W. 1994, ApJ, 437, 879
 Arnett, D., 1972, ApJ, 173, 393
 Arnett, D. 1996, Supernovae and Nucleosynthesis: An Investigation of the History of Matter, from the Big Bang to the Present, by D. Arnett. Princeton: Princeton University Press, 1996
 Asplund, M., Grevesse, N., & Sauval, A. J. 2005, in ASP Conf. Ser. 336, Cosmic Abundances as Records of Stellar Evolution and Nucleosynthesis, ed. T. G. Barnes III & F. N. Bash (San Francisco: ASP), in press (astro-ph/0410214)
 Aufderheide, M. B. 1993, ApJ, 411, 813
 Beaudet, G., Petrosian, V., & Salpeter, E. E. 1967, ApJ, 150, 979
 Belkacem, K., Samadi, R., Goupil, M. -, & Kupka, F. 2006, ArXiv Astrophysics e-prints, arXiv:astro-ph/0607568
 Böhm-Vitense, E., 1958, ZAp, 46, 108
 Böhm-Vitense, E. 1992, Introduction to Stellar Astrophysics, by Erika Böhm-Vitense, pp. 301. ISBN 05 21348714. Cambridge, UK: Cambridge University Press, January 1992.
 Bretherton, C. et al. 1999, Quart. J. Roy. Meteor. Soc., 125, 391
 Carruthers, D. J., & Hunt, J. C. R. 1986, Journal of Fluid Mechanics, 165, 475
 Cattaneo, F., Brummell, N. H., Toomre, J., Malagoli, A., & Hurlburt, N. E. 1991, ApJ, 370, 282
 Chan, K. L., & Sofia, S. 1987, Science, 235, 465
 Chan, K. L., & Sofia, S. 1989, ApJ, 336, 1022
 Chan, K. L., & Sofia, S. 1996, ApJ, 466, 372
 Clayton, D. D. 1983, *Principles of Stellar Evolution and Nucleosynthesis*, University of Chicago Press, Chicago
 Colella, P., & Glaz, H. M. 1985, Journal of Computational Physics, 59, 264
 Colella, P., & Woodward, P., 1984, J. Chem. Phys., 54, 174
 Cox, J. P., & Guili, R. T., 1968, *Principles of Stellar Structure*, New York: Gordon & Breach
 Deardorff, J. W. 1979, Journal of Atmospheric Sciences, 36, 424
 Deardorff, J. W. 1980, Journal of Atmospheric Sciences, 37, 131
 Fedorovich, E. E., Conzemius, R., & Mironov, D. V. 2004, Journal of Atmospheric Sciences, 61, 281
 Fedorovich, E. E., & Mironov, D. V. 1995, Journal of Atmospheric Sciences, 52, 83
 Fernando, H. J. S. 1991, Annual Review of Fluid Mechanics, 23, 455
 Fernando, H. J. S., & Hunt, J. C. R. 1997, Journal of Fluid Mechanics, 347, 197
 Ferraro, F. R., Valenti, E., Straniero, O., and Origlia, L., 2006, ApJ, 642, 225
 Fryxell, B., Müller, E., & Arnett, D., 1989, ApJ367, 619
 Fryxell, B., et al. 2000, ApJS, 131, 273
 Gough, D. O. 1969, Journal of Atmospheric Sciences, 26, 448
 Grevesse, N. & Sauval, A. J., 1998, Space Science Reviews, 85, 161
 Hansen, C. J., & Kawaler, S. D., 1994, *Stellar Interiors*, Springer-Verlag
 Herwig, F., Freytag, B., Hueckstaedt, R. M., & Timmes, F. X. 2006, ApJ, 642, 1057
 Hoyle, F. 1946, MNRAS, 106, 343
 Iglesias, C. & Rogers, F. J. 1996, ApJ, 464, 943
 Itoh, N., Hayashi, H., Nishikawa, A., & Kohyama, Y. 1996, ApJS, 102, 411
 Kantha, L. H., Phillips, O. M., & Azad, R. S. 1977, Journal of Fluid Mechanics, 79, 753
 Kim, Y.-C., Fox, P. A., Demarque, P., & Sofia, S. 1996, ApJ, 461, 499
 Kim, Y.-C., Fox, P. A., Sofia, S., & Demarque, P. 1995, ApJ, 442, 422
 Kippenhahn, R. & Weigert, A. 1990, *Stellar Structure and Evolution*, Springer-Verlag
 Knobloch, E., & Merryfield, W. J. 1992, ApJ, 401, 196
 Lattanzio, J. C., & Lugaro, M. A. 2005, Nuclear Physics A, 758, 477
 Lesaffre, P., Podsiadlowski, P., & Tout, C. A. 2005, MNRAS, 356, 131
 Lewellen, D. C., & Lewellen, W. S. 1998, Journal of Atmospheric Sciences, 55, 2645
 Linden, P. F. 1975, Journal of Fluid Mechanics, 71, 385
 McGrath, J. L., Fernando, H. J. S., & Hunt, J. C. R. 1997, Journal of Fluid Mechanics, 347, 235
 Meakin, C., & Arnett, D. 2006, ApJ, 637, 53
 Meakin, C., & Arnett, D. 2006, submitted.
 Phillips, O. M. 1966, *The Dynamics of the Upper Ocean*, Cambridge University Press. N.Y.
 Porter, D. H., Woodward, P. R., & Jacobs M. L., in *Astrophysical Turbulence and Convection*, Ann. N. Y. Acad. Sci., 898
 Porter, D. H., & Woodward, P. R. 2000, ApJS, 127, 159
 Press, W. H. 1981, ApJ, 245, 286
 Rauscher, T., & Thielemann, K.-F., 2000, Atomic Data Nuclear Data Tables, 75, 1
 Rempel, M. 2004, ApJ, 607, 1046
 Robinson, F. J., Demarque, P., Li, L. H., Sofia, S., Kim, Y.-C., Chan, K. L., & Guenther, D. B. 2003, MNRAS, 340, 923
 Robinson, F. J., Demarque, P., Li, L. H., Sofia, S., Kim, Y.-C., Chan, K. L., & Guenther, D. B. 2004, MNRAS, 347, 1208
 Robinson, F. J., Demarque, P., Guenther, D. B., Kim, Y.-C., & Chan, K. L. 2005, MNRAS, 362, 1031
 Smagorinsky, J. S., 1963, Mon. Weather Rev., 91, 99
 Sorbjan, Z. 1996, Journal of Atmospheric Sciences, 53, 101

- Staquet, C., & Sommeria, J. 2002, *Annual Review of Fluid Mechanics*, 34, 559
- Stevens, B. 2002, *Quarterly Journal of the Royal Meteorological Society*, 128, 2663
- Stevens, D. E., & Bretherton, C. S. 1999, *Quarterly Journal of the Royal Meteorological Society*, 125, 425
- Strang, E. J., & Fernando, H. J. S. 2001, *Journal of Fluid Mechanics*, 428, 349
- Stull, R. B. 1973, *Journal of Atmospheric Sciences*, 30, 1092
- Stull, R. B. 1976, *Journal of Atmospheric Sciences*, 33, 1260
- Stull, R. B. 1976, *Journal of Atmospheric Sciences*, 33, 1268
- Styne, I., Porter, D. H., Woodward, P. R., Hodson, S. H., Winkler, K. H., 2000, *J. Chem. Phys.*158, 225
- Tennekes, H. 1974, *Journal of Atmospheric Sciences*, 30, 558
- Timmes, F. X. & Swesty, F. D. 2000, *ApJS*, 126, 501
- Turner, J. S. 1980, *Buoyancy Effects in Fluids*, by J. S. Turner, pp. 382. ISBN 0521297265. Cambridge, UK: Cambridge University Press, January 1980
- Unno, W., Osaki, Y., Ando, H., Saio, H., & Shibahashi, H. 1989, *Nonradial oscillations of stars*, Tokyo: University of Tokyo Press, 1989, 2nd ed.,
- Young, P. A. & Arnett, D. 2005, *ApJ*, 618, 908
- Zahn, J.-P. 1991, *A&A*, 252, 179

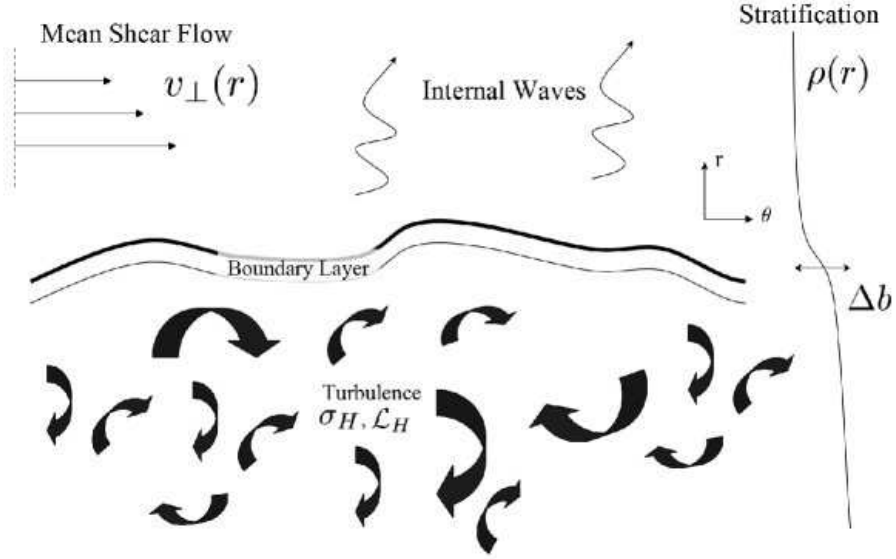


FIG. 1.— Diagram illustrating the salient features of the density and velocity field for the turbulent entrainment problem. Three layers are present: a turbulent convection zone is separated from an overlying stably stratified region by a boundary layer of thickness h and buoyancy jump $\Delta b \sim N^2 h$. The turbulence near the interface is characterized by integral scale and RMS velocity \mathcal{L}_H and σ_H , respectively. The stably stratified layer with buoyancy frequency $N(r)$ propagates internal waves which are excited by the adjacent turbulence. A shear velocity field $v_\perp(r)$, associated with differential rotation, may also be present. After Strang & Fernando (2001).

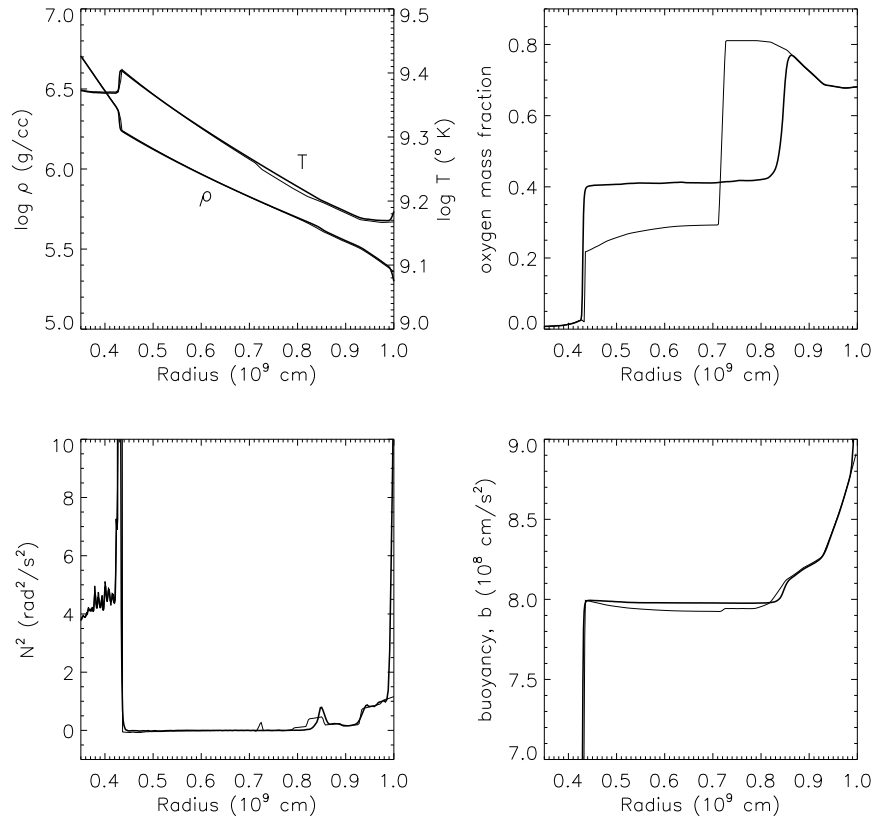


FIG. 2.— Radial profile of the simulated region for the oxygen shell burning models. The thin lines indicate the initial conditions and the thick lines indicate the 3D model at $t = 400$ s. (top left) Temperature and density. (top right) Mass fraction of ^{16}O . (bottom left) Squared buoyancy frequency. (bottom right) Buoyancy.

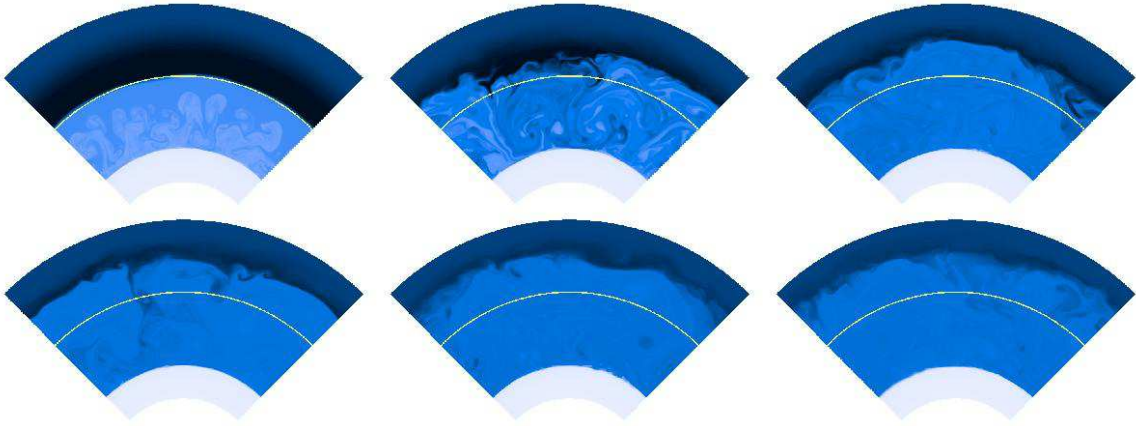


FIG. 3.— This time sequence shows the onset of convection in the oxygen shell burning model. The first 200 s of the 2D model (ob,2d.c) is shown, including the initial transient and the settling down to a new quasi-steady state. The light yellow line indicates the location of the convective boundary as defined in the 1D TYCHO stellar evolution model (Ledoux criterion), which was used as initial conditions for the simulation.

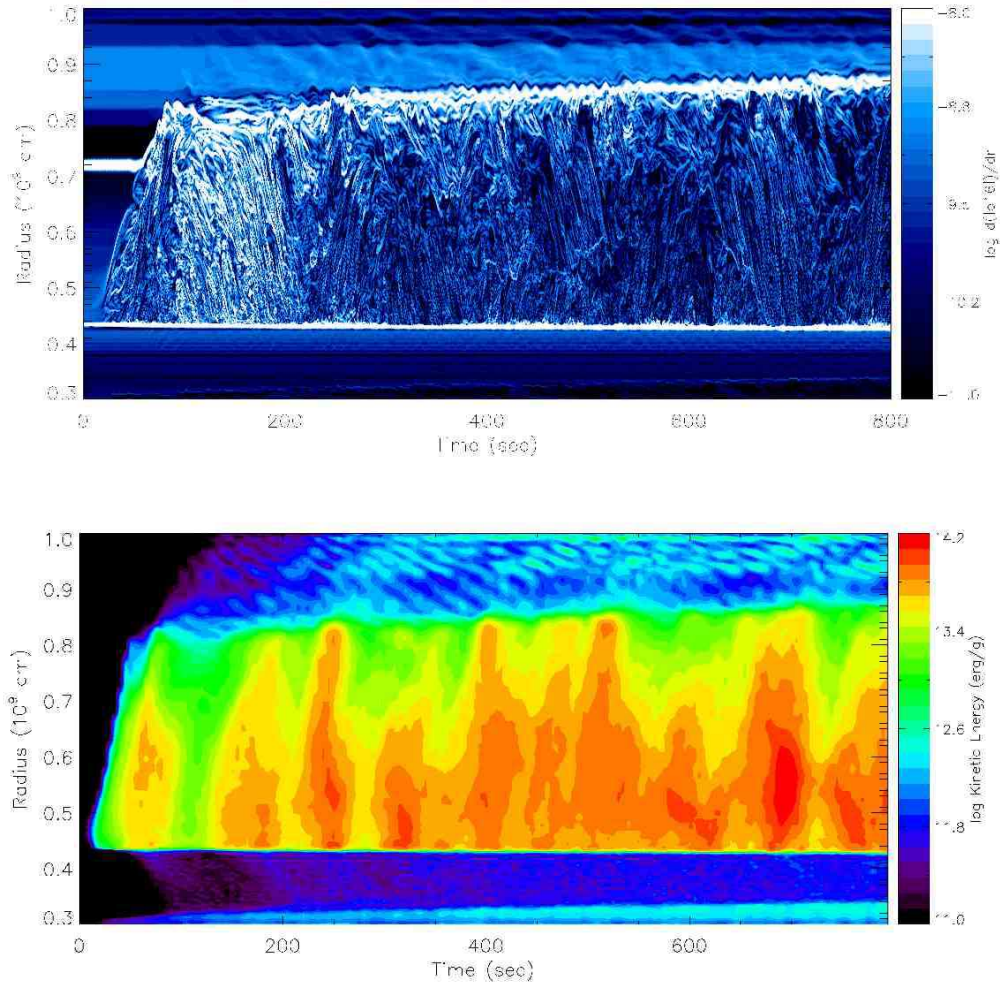


FIG. 4.— The time evolution of the 3D oxygen shell burning model. (top) The magnitude of the oxygen abundance gradient is shown and illustrates the migration of the convective boundaries into the surrounding stable layers. Interfacial oscillations are also apparent in the upper convective boundary layer ($r \sim 0.85 \times 10^9$ cm), and internal wave motions can be seen quite clearly in the upper stable layer. (bottom) The kinetic energy density is shown, and illustrates the intermittent nature of the convective motions. The upwelling chimney-like features in the convective region are seen to excite internal wave trains in the stable layers, which propagate away from the boundaries of the convection zones. See also Fig. 25.

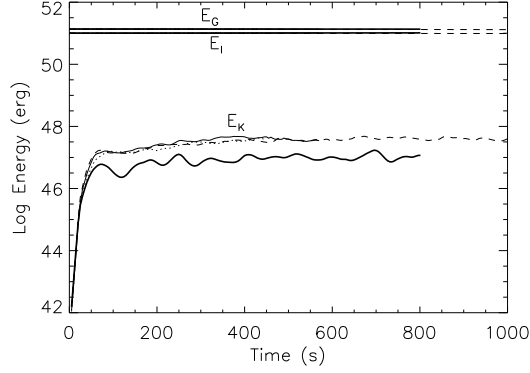


FIG. 5.— The time evolution of the energy budgets for the oxygen shell burning models: the (thick line) 3D model, and (thin lines) the three 2D models are shown, including: (thin-solid) ob.2d.c; (thin-dashed) ob.2d.e; and (thin dotted) ob.2d.C. The energy budget includes the internal energy E_I , the gravitational energy E_G , and the kinetic energy E_K . Note that the energy scale is logarithmic, so that the 3D kinetic energy is much smaller than the 2D values.

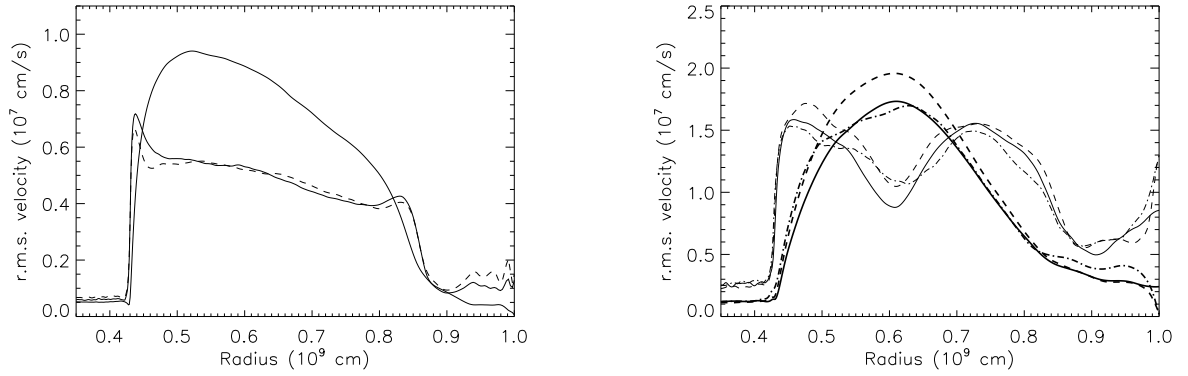


FIG. 6.— The r.m.s. velocity fluctuations for oxygen shell burning: (left) 3D model, with velocity components (thick-solid) v_r , (thin-solid) v_θ , and (thin-dashed) v_ϕ . (right) The 2D models, with velocity components (thick) v_r and (thin) v_ϕ for simulations (solid) ob.2d.e, (dashed) ob.2d.c, and (dash-dot) ob.2d.C.

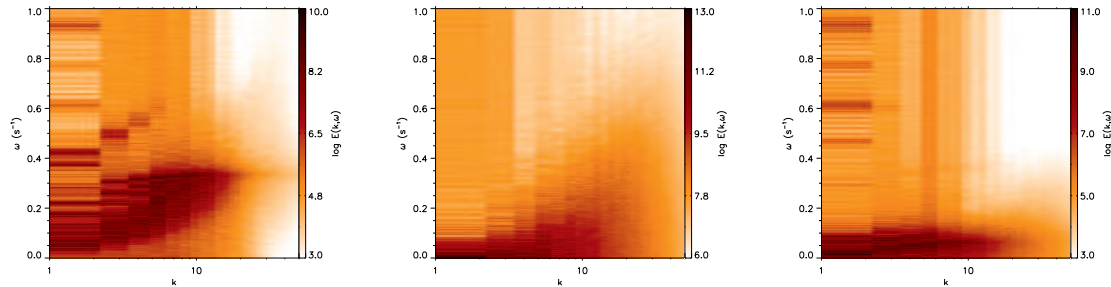


FIG. 7.— Mode diagrams for several radial positions in the oxygen shell burning model show the dominant spatial and time scales on which motions occur. The abscissa measures k which is related to the wavenumber index l of the mode by $l = 12 \times k$. The three locations shown here include: (left) Lower stable layer, just beneath the convective shell $r = 0.4 \times 10^9$ cm. (middle) Middle of convective shell, $r = 0.6 \times 10^9$. (right) Upper stable layer, just above the convective shell $r = 0.9 \times 10^9$ cm.

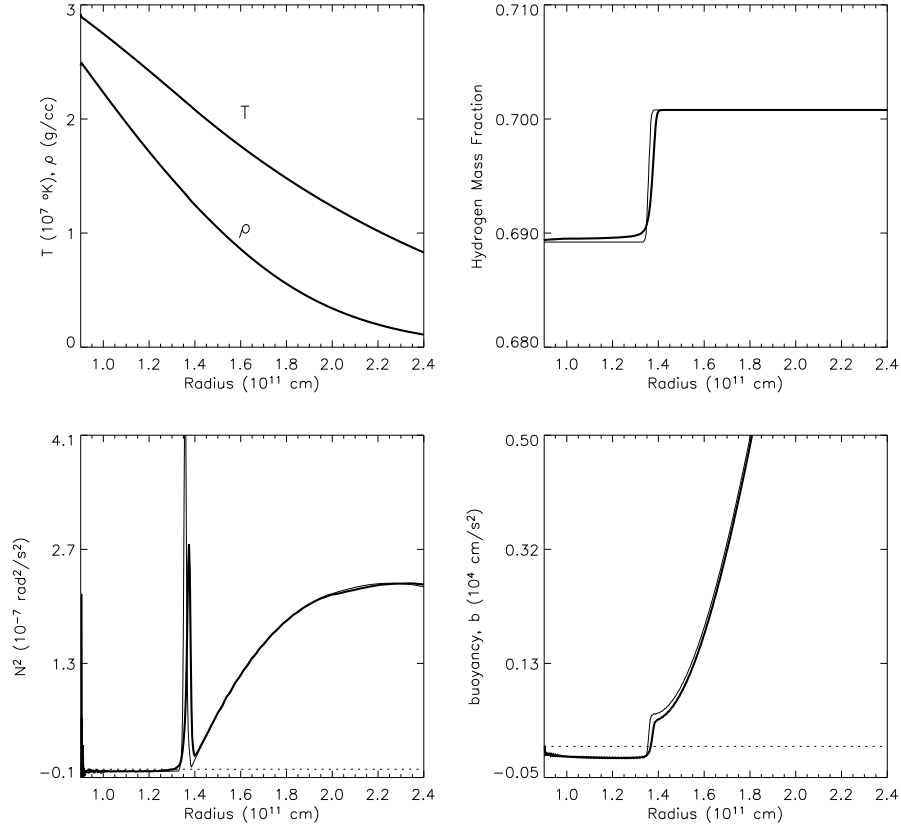


FIG. 8.— Radial profile of the simulated region for the main sequence core convection model. The thin lines show the initial conditions and the thick lines show the state of the 3D model at $t = 10^6$ s. (top left) Temperature and density. (top right) Hydrogen abundance. (bottom left) Squared buoyancy frequency. (bottom right) Buoyancy.

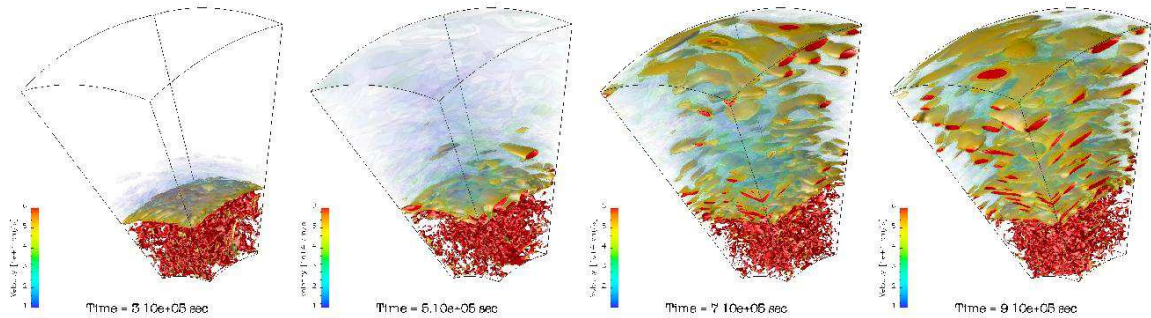


FIG. 9.— Velocity isocontours show the development of the flow in the 3D core convection model. The turbulent convective flow excites internal waves which radiate into the overlying stably stratified layer. By the end of the time sequence shown the stable layer cavity is filled with resonant modes.

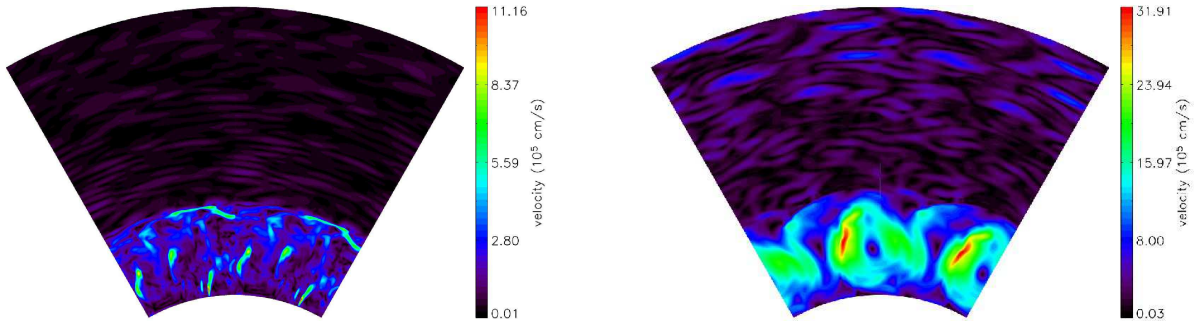


FIG. 10.— The velocity magnitude for the core convection model at $t=10^6$ s: (left) a slice through the 3D model; and (right) the 2D model. The topology of the convective flow is significantly different between 2D and 3D models: the 3D convective flow is dominated by small plumes and eddies while the 2D flow is much more laminar, and dominated by a large vortical eddies which span the depth of the layer. The wave motions in the stable layer have similar morphology in 2D and 3D, but the velocity amplitudes are much larger in 2D. The computational domains have been tiled once in angle for presentation.

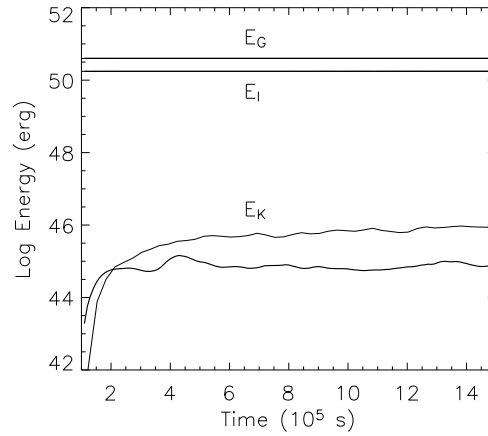


FIG. 11.— The time evolution of the energy budget for the main sequence core convection models: the (thick line) 3D model; and (thin line) the 2D model are shown. The energy budget includes the total internal energy E_I , gravitational energy E_G , and kinetic energy E_K on the computational grid.

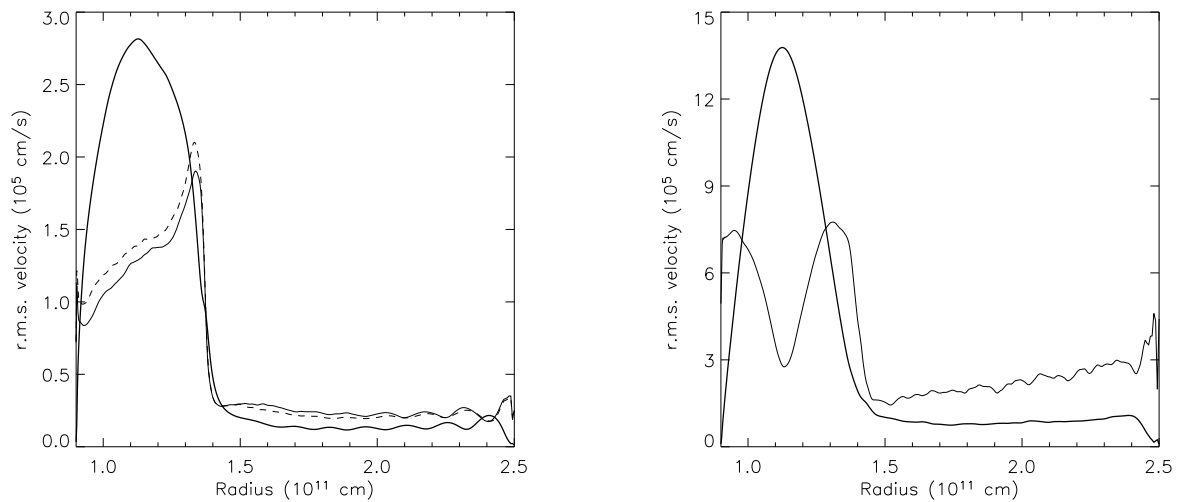


FIG. 12.— The r.m.s. velocity fluctuations for the core convection model: (left) the 3D model, and (right) the 2D model. In each plot, the thick line indicates the radial velocity component and thin line is used to indicate horizontal velocity components, with the dashed line used to show the polar angle component in the 3D model.

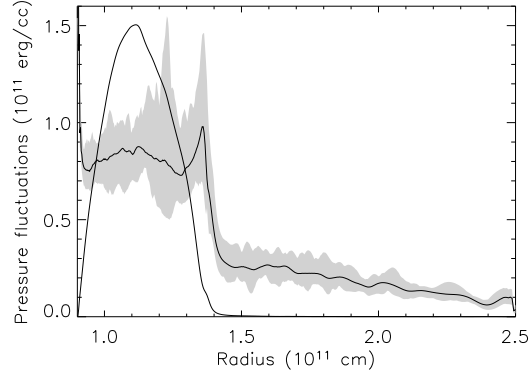


FIG. 13.— Pressure fluctuations in core convection model: The time averaged horizontal r.m.s. pressure fluctuations are shown as the thick line, with extreme values over two convective turnovers indicated by the shaded region. The thin line shows the radial component of the turbulent ram pressure ρv_r^2 averaged over a convective turnover. At the upper boundary, the curves cross at a point where the turbulent pressure is balanced by the wave induced pressure fluctuations in the stable layer. This crossing point is coincident with the location of the convective boundary. The pressure perturbations at the lower boundary are due to the input luminosity which drives the convective flow.

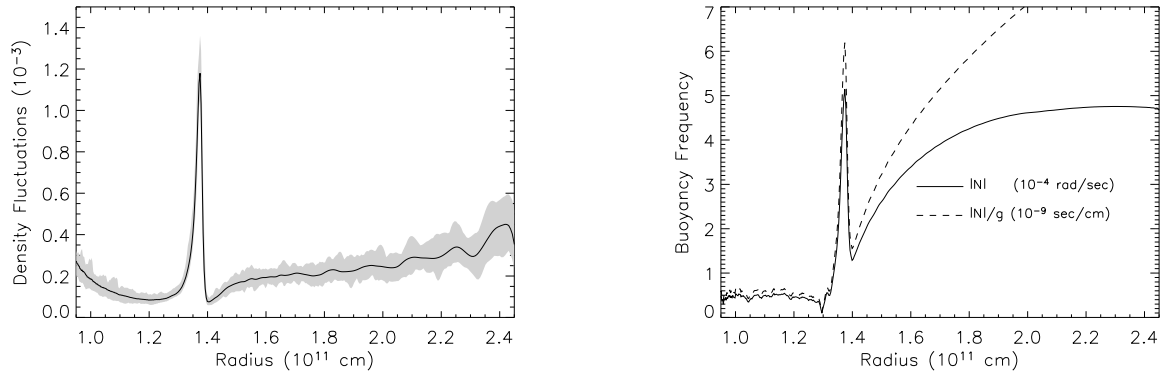


FIG. 14.— (left) Density fluctuations in the 3D core convection model: The time averaged maximum density fluctuation is shown as the thick line, with extreme values for the averaging period (two convective turnovers) shown by the shaded region. The largest fluctuations occur at the interface between the turbulent convective region and the stably stratified layer. The maximum fluctuation at the interface is $\rho'/\langle\rho\rangle \sim 0.12\%$. (right) The buoyancy frequency is shown in units of (10^{-4} rad/sec). Also shown by the dashed line is the buoyancy frequency normalized by the gravity which sets the scale of the density fluctuations at the convective boundary through equation 13. The expected density fluctuation is $\rho'/\langle\rho\rangle \sim v_c|N|/g \sim 0.12\%$, where a velocity scale of $v_c \sim 2 \times 10^5$ cm/s has been used (see Figure 12).

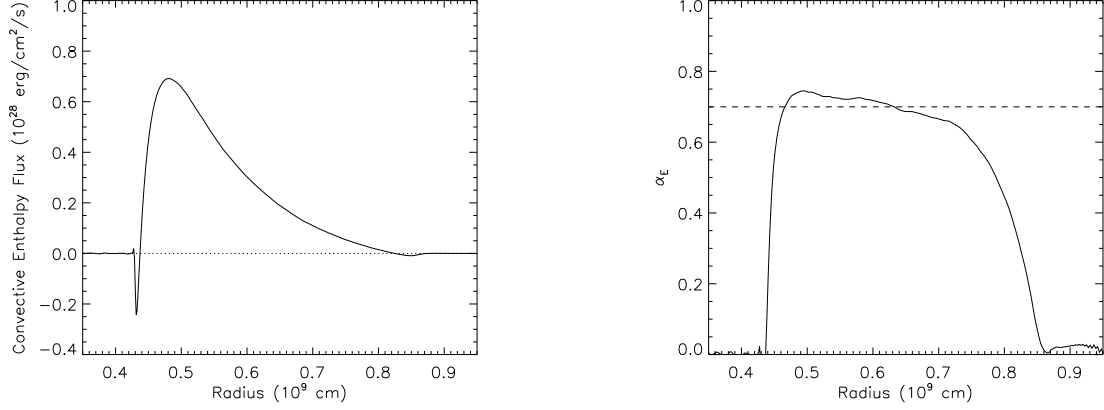


FIG. 15.— (left) Convective enthalpy flux, $F_c = \overline{\langle \rho c_p v_r T' \rangle}$. (right) Temperature-velocity correlation function α_E calculated according to equation 21, with mean value $\langle \alpha_E \rangle = 0.7$ shown by the dashed line.

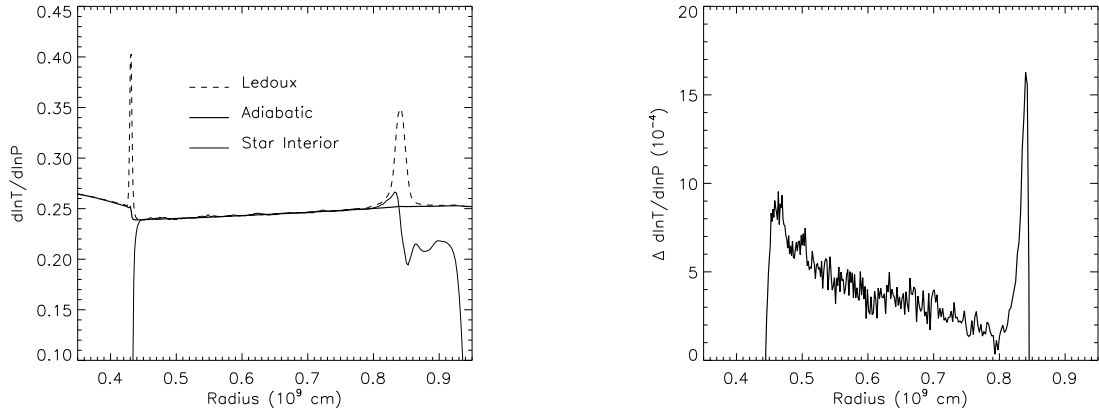


FIG. 16.— (left) Dimensionless temperature gradients: the stellar interior ∇_s ; adiabatic ∇_{ad} ; and Ledoux ∇_{led} gradients are shown. (right) Super-adiabatic temperature gradient horizontally and time averaged.

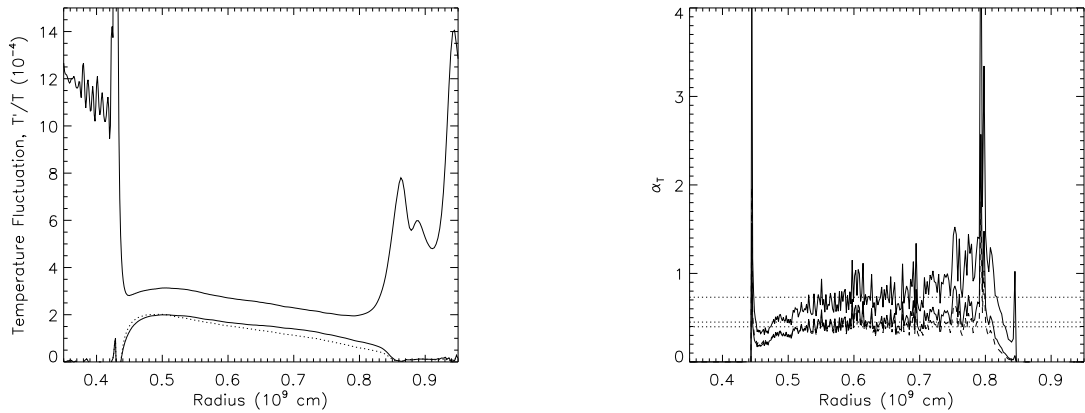


FIG. 17.— (left) Time averaged r.m.s. temperature fluctuations: (thick solid) line shows the r.m.s. fluctuations; the (thin solid) and (thin dotted) lines show the fluctuations in the upward and downward directed flow components, respectively. (right) The radial dependence of the "thermal mixing length" parameters α_T defined by equation 22 are shown the temperature fluctuations presented in the left panel, using the same line types. The mean values, averaged over $r \in [0.5, 0.75] \times 10^9$ cm are shown by the thin dotted lines.

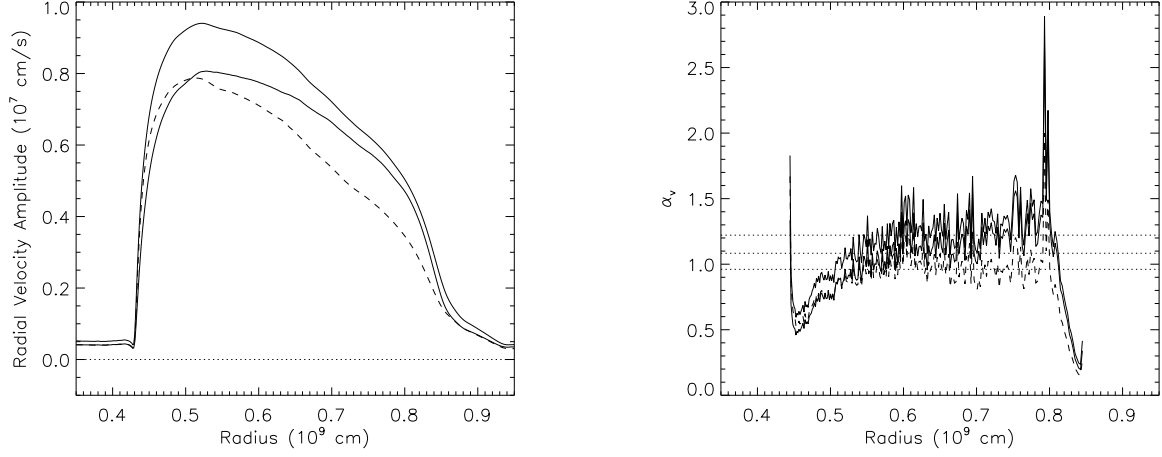


FIG. 18.— (left) Radial velocity amplitudes: (thick solid) r.m.s. value; the (thin solid) and (thin dashed) show the mean up- and down-flow velocities, respectively. (right) The radial dependance of the "velocity mixing length" parameters α_v defined by equation 23 are shown for the velocity amplitudes presented in the left panel, using the same line types. The mean values, averaged over $r \in [0.5, 0.75] \times 10^9 \text{cm}$ are shown by the thin dotted lines.

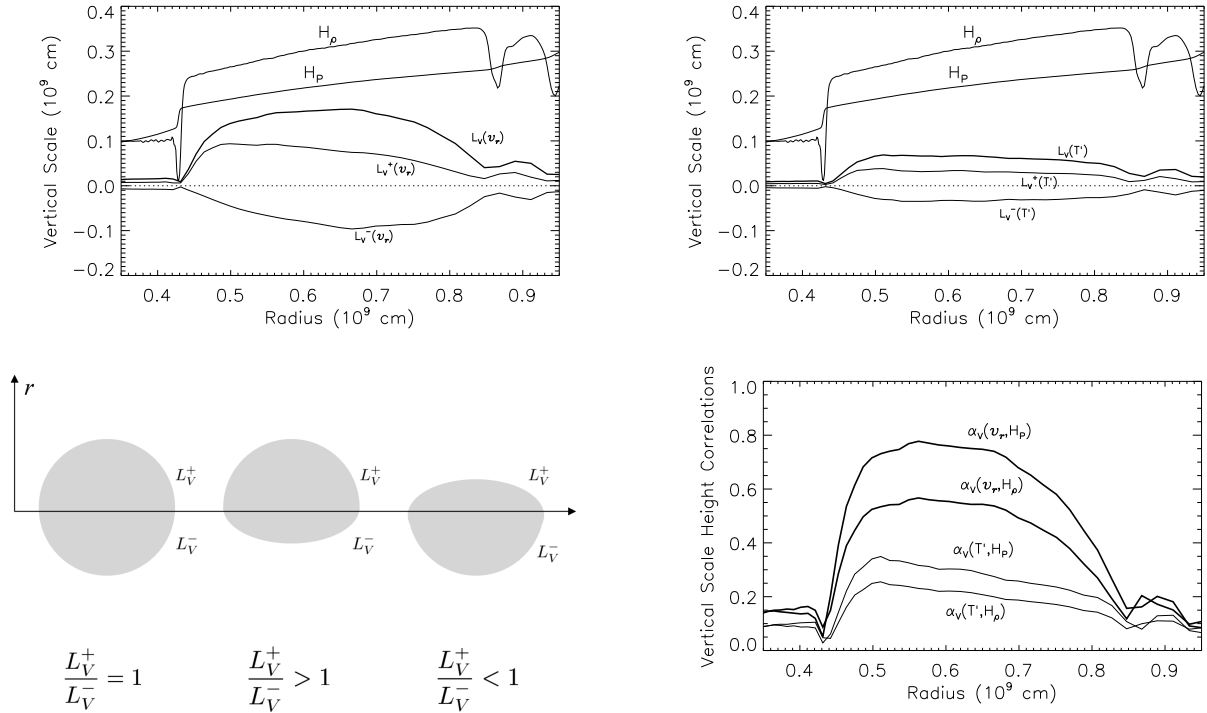


FIG. 19.— The vertical correlation length scales L_V as defined in §B. (top left) L_V for velocity fluctuations, v'_r ; (top right) L_V for temperature fluctuations, T' . The pressure scale height H_p and density scale height H_ρ are shown for comparison. (bottom left) Illustration of the relationship between eddy shape and the correlation length scales, L_V^+ and L_V^- . The grey patches represent the shapes of the eddies and the $L_V^{+/-}$ values are measured in the radial direction, away from the horizontal line. (bottom right) Correlations lengths L_V scaled to pressure and density scale heights, e.g., $\alpha_V(v_r, H_p) = L_V(v_r)/H_p$

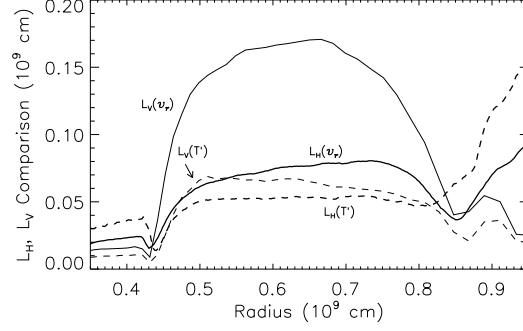


FIG. 20.— The horizontal and vertical correlation length scales, L_H (thick line) and L_V (thin line) are shown for temperature (dashed) and velocity (solid) fluctuations.

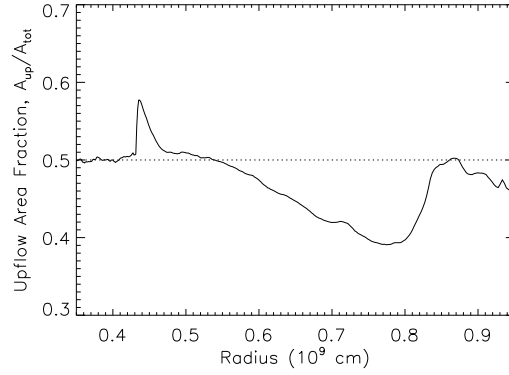


FIG. 21.— The fractional area occupied by the upward flowing material f_u is shown as a function of radial position. The downward flowing area is $f_d = (1 - f_u)$ and the dashed line at $1/2$ indicates up-down symmetry.

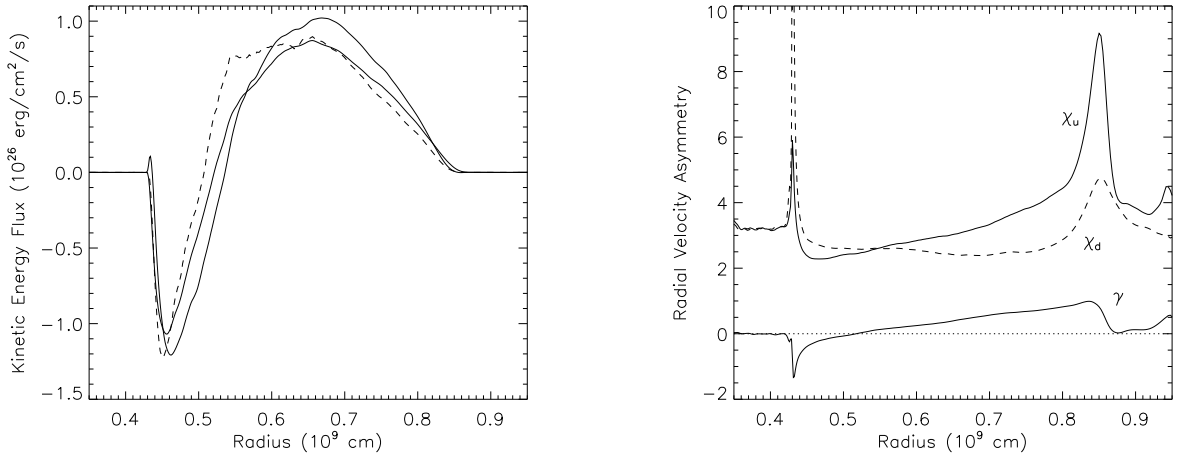


FIG. 22.— (left) Kinetic energy flux: (thick) line shows the value measured in the simulation averaged over two convective turnovers; the (thin solid) line shows F_K calculated according to equation 26; the (thin dashed) line shows F_K calculated according to equation 26 but uses $c\langle v \rangle^3$ in place of $\langle v^3 \rangle$, and a correlation constant of $c = 5$. (right) Asymmetries in radial velocity: the (thick) line show the skewness in the velocity field, $\gamma = \langle v^3 \rangle / \sigma_v^3$; the (thin solid) and (thin dashed) lines show the correlations $\chi = \langle v^3 \rangle / \langle v \rangle^3$ where the subscripts u and d indicate up- and down-flows, respectively.

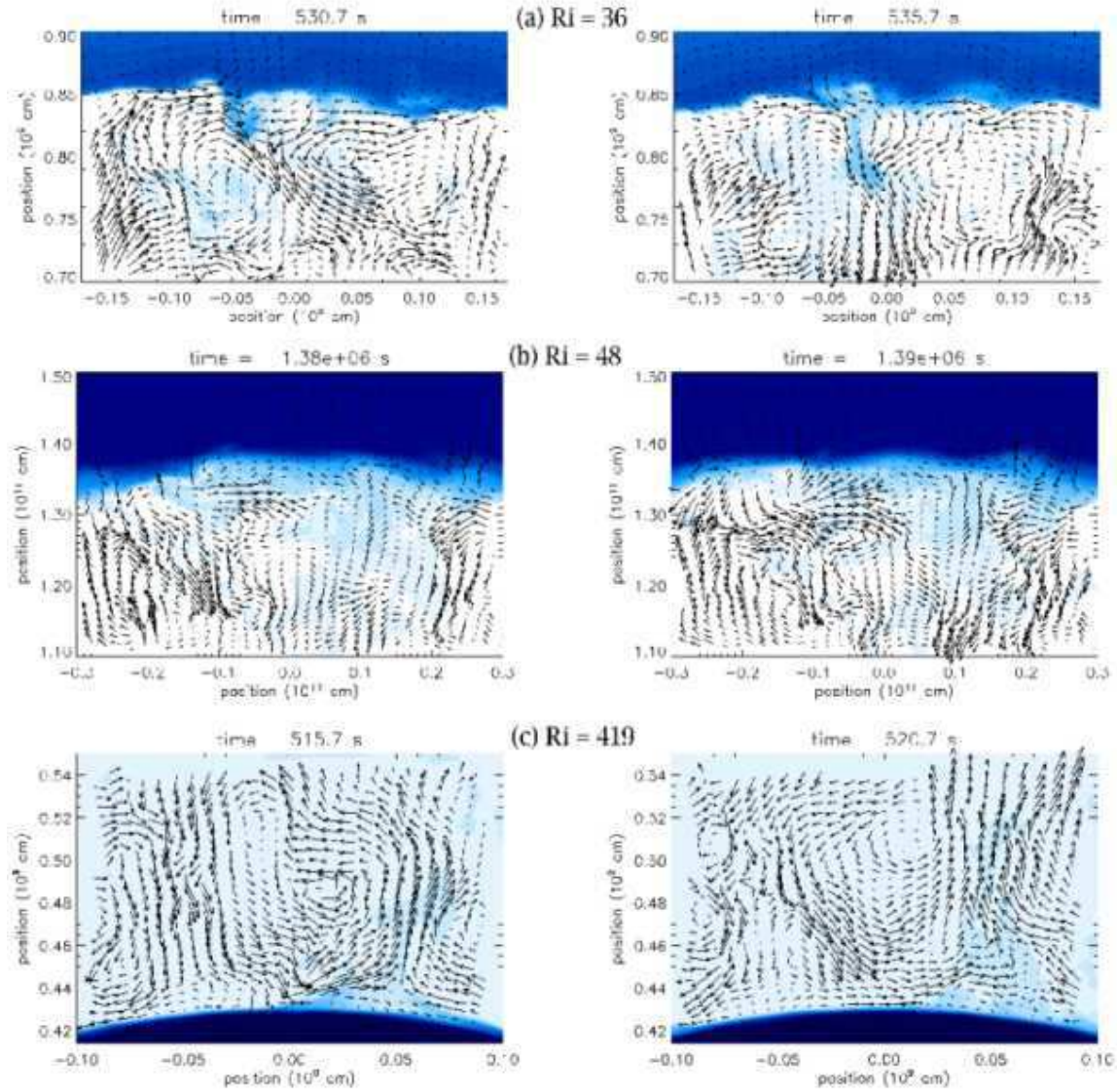


FIG. 23.— Equatorial slices showing the flow in the vicinity of the convective boundaries in the 3D simulations, ordered by relative stability: (row a) upper shell convection boundary, $Ri_B \sim 36$; (row b) core convection boundary, $Ri_B \sim 48$; (row c) lower shell convection boundary, $Ri_B \sim 419$. The colormap indicates composition abundance, where the darker tones trace stable layer material entrained across the interface. The velocity vectors have been sampled every third zone in each dimension.

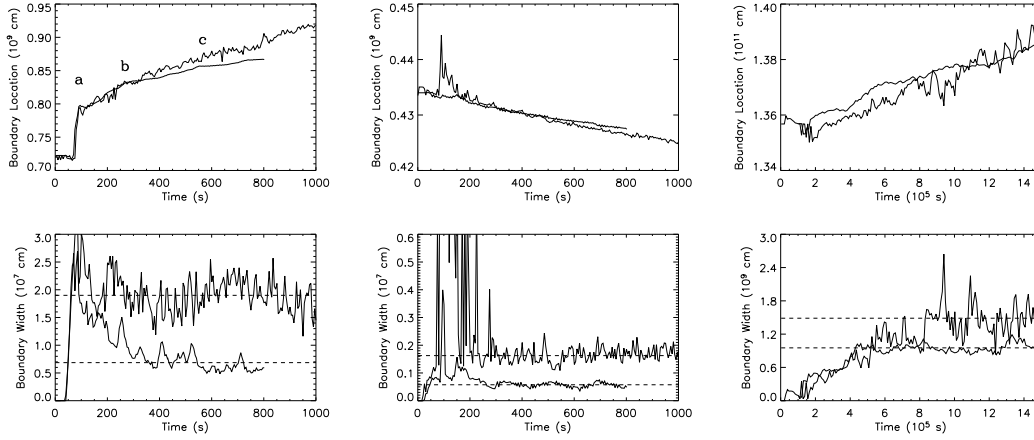


FIG. 24.— The time history of (top row) the convective boundary location, and (bottom row) the thickness of the convective interface for: (left) upper shell burning boundary; (middle) lower shell burning boundary; and (right) core convection boundary. The (thick line) identifies the 3D models, ob.3d.B and msc.3d.B; and the (thin line) identifies the 2D models, ob.2d.e and msc.2d.b. The (dashed lines) show the averaged interface thickness for $t > 300$ s for oxygen burning, and $t > 6.0 \times 10^5$ s for core convection. The letters (a-c) in the upper left panel mark times when the outward migration rate of the convective boundary rapidly adjusts to a new value in the 3D model.

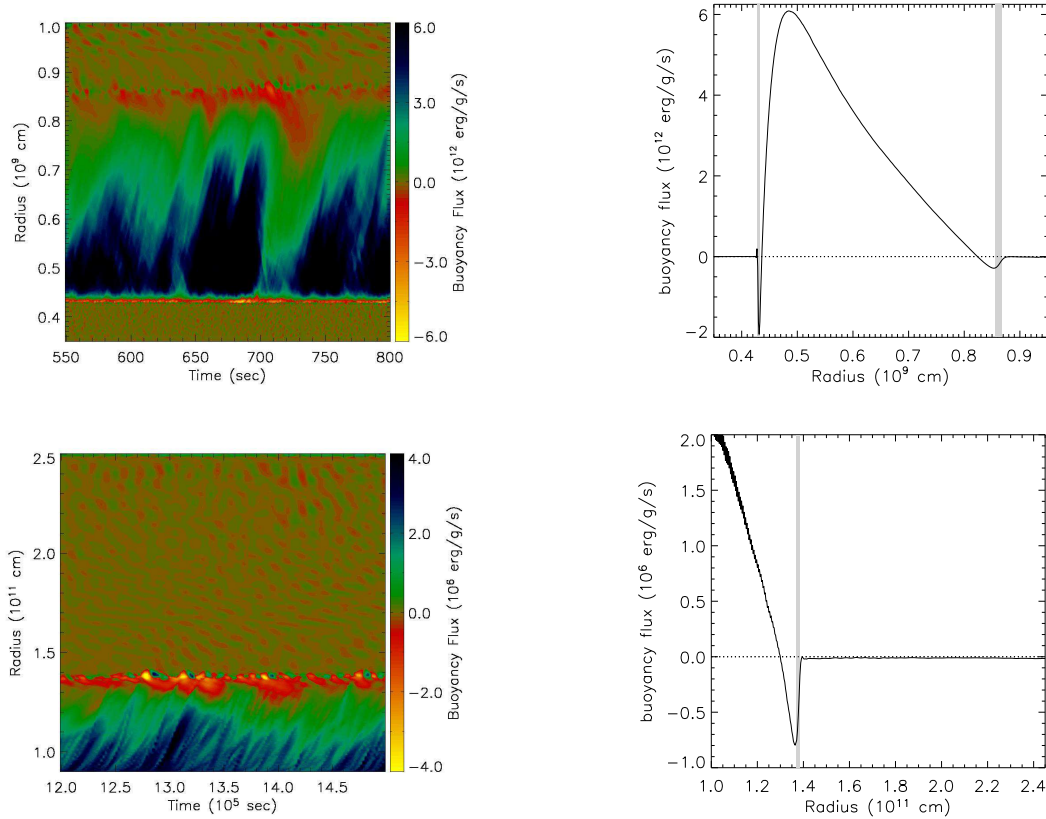


FIG. 25.— Buoyancy flux. Time-series diagrams and time-averaged radial profiles are shown for: (top-row) the 3D oxygen shell burning model; and (bottom-row) the 3D core convection model.

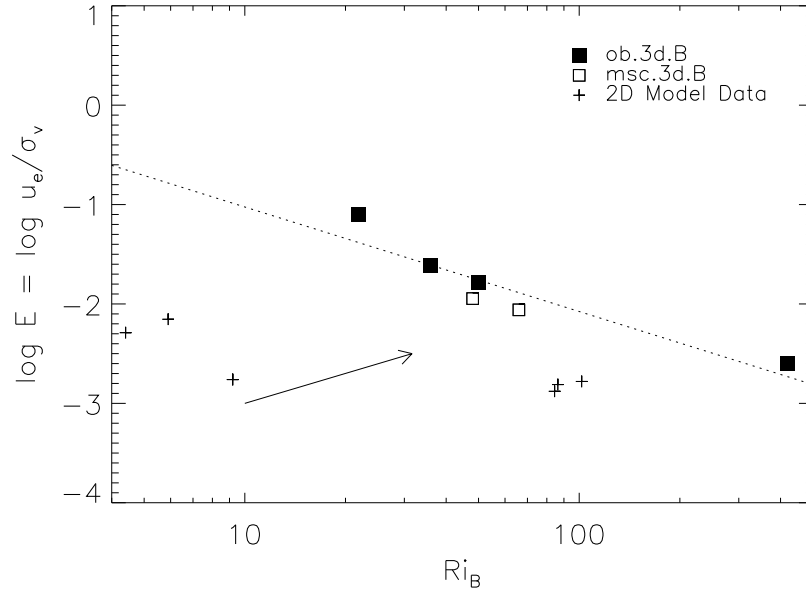


FIG. 26.— Normalized entrainment rate plotted against bulk Richardson number Ri_B . The 3D models are marked with squares, and the 2D data by plus signs. The best fit power-law to the 3D model data is shown by the dashed line. The 2D entrainment rates fall everywhere below the 3D trend. The arrow indicates the direction in the diagram that the 2D data points would move if the effective r.m.s. turbulence velocity were lower.

TABLE 1
NUCLEI INCLUDED IN REDUCED
NUCLEAR REACTION NETWORK

Element	Charge	Atomic Weight
Helium	2	4
Carbon	6	12
Oxygen	8	16
Neon	10	20
Sodium	11	23
Magnesium	12	24
Silicon	14	28
Phosphorus	15	31
Sulfur	16	32, 34
Chlorine	17	35
Argon	18	36, 38
Potassium	19	39
Calcium	20	40, 42
Titanium	22	44, 46
Chromium	24	48, 50
Iron	26	52, 54
Nickel	28	56

NOTE. — Network also includes electrons, protons, and neutrons.

TABLE 2
SUMMARY OF OXYGEN SHELL BURNING MODELS

Parameter	Units	ob.3d.B	ob.2d.c	ob.2d.C	ob.2d.e
r_{in}, r_{out}	(10^9 cm)	0.3, 1.0	0.3, 1.0	0.3, 1.0	0.3, 5.0
$\Delta\theta, \Delta\phi$	(deg.)	30, 30	90, 0	90, 0	90, 0
Grid Zoning	-	$400 \times (100)^2$	400×320	800×640	800×320
t_{max}	(s)	800	574	450	2,400
v_{conv}	(10^7 cm/s)	0.8	2.0	1.8	1.8
t_{conv}	(s)	103	40	44	44
$\dot{M}_i _u$ ¹	($10^{-4} M_\odot/s$)	1.1	1.33	1.25	1.3
$\dot{M}_i _l$	($10^{-4} M_\odot/s$)	-0.23	-0.52	-0.5	-0.5

¹The subscripts u and l refer to the upper and lower convective shell boundary.

TABLE 3
SUMMARY OF “CORE CONVECTION” MODELS

Parameter	Units	msc.3d.B	msc.2d.b
r_{in}, r_{out}	(10^{11} cm)	0.9, 2.5	0.9, 2.5
$\Delta\theta, \Delta\phi$	(deg.)	30, 30	30, 0
Grid Zoning	-	$400 \times (100)^2$	400×100
t_{max}	(s)	2.0×10^6	2.0×10^6
v_{conv}	(10^5 cm/s)	2.5	13
t_{conv}	(s)	3.6×10^5	6×10^4
\dot{M}_i	($10^{-7} M_\odot/s$)	2.72	4.73

TABLE 4
 ASSUMED AND MEASURED CONVECTION PARAMETERS^a

Study	Pé ^b	α_E	$\alpha_{\Lambda,T}$	$\alpha_{\Lambda,v}$	α_Λ	L/H_p^c	Grid Zoning
MLT	$\gg 1$	1	α	α	α
This Study ¹	$\gtrsim 10^3$	0.70±0.03	0.8 - 1.4	1.35 - 1.73	0.87 - 1.31	$\sim 2(3.7)^d$	$100^2 \times 223(400)^c$
Chan-Sofia ²	...	0.81±0.03	1.32 - 3.75	3.39 - 6.4	1.90 - 4.4	7	$20^2 \times (\lesssim 50)$
Kim ³	...	0.80±0.01	2.96 - 4.2	1.5 - 3.4	1.4 - 3.2	6	32^3
Robinson ⁴	...	0.65-0.85	8.5	$114^2 \times 170$
Porter-Woodward ^{5a}	$10 - 8 \times 10^4$	0.7-0.9	4.08	3.82	2.68(3.53) ^{5b}	5	$512^2 \times 256$

^aSee §6.2 for parameter definitions: $\alpha_{\Lambda,T} = 2 \times \alpha_T$ and $\alpha_{\Lambda,v} = \sqrt{2} \times \alpha_v$ where α_T and α_v are defined by equations 22 and 23, and $\alpha_\Lambda = \sqrt{\alpha_E \times \alpha_{\Lambda,v} \times \alpha_{\Lambda,T}}$.

^bThe Péclet number is shown when provided by the author. In all cases the regions in the simulations for which parameter values are quoted were efficient convection, with $\Delta\nabla \lesssim 10^{-2}$, and excluded the super-adiabatic layers in the surface convection models where parameters deviate significantly from those quoted here.

^cThe number of pressure scale heights spanned by the convectively unstable region.

^dThe value in parentheses is for region spanning the entire computational domain, including the stable bounding layers with the other value referring to the convective region.

¹Model ob.3d.B: additional details in Table 2.

²Chan & Sofia (1989): The range in α_T and $\alpha_{\Lambda,v}$ is calculated according to their Table 1 for the nearly adiabatic portion of the simulation where $10^{-3} < \Delta\nabla < 10^{-2}$.

³Kim et al. (1996): The coefficient α_T is based on their Fig. 6. The coefficients $\alpha_{\Lambda,v}$ and α_Λ are plotted in their Fig. 9 and the range quoted in the table above is for values at least one pressure scale height from the boundaries.

⁴Robinson et al. (2004): only the correlation between radial velocity and temperature fluctuation is provided, which is a good surrogate for α_E . For the solar and subgiant cases see their Figs. 7 - 9.

⁵(a)Porter & Woodward (2000): In this paper the values for α_v , α_T , and α_Λ are quoted using the same definitions as in this study. (b) The lower value quoted by these authors for α_Λ is a results of subtracting the kinetic energy flux from the enthalpy flux. The value in the parentheses is the mixing length α_Λ according to the definition in note ^a above.

 TABLE 5
 CONVECTIVE BOUNDARY LAYER PROPERTIES FOR OXYGEN SHELL BURNING MODELS

Model	Time Interval (10^2 s)	\bar{r}_i (10^9 cm)	\bar{h} (10^7 cm)	\bar{r}_i (10^4 cm/s)	$\overline{v_{exp}}$ (10^4 cm/s)	$\sigma[v_H]^a$ (10^7 cm/s)	$\overline{\Delta b}^b$ (10^7 cm/s ²)	$\log \bar{E}$	\overline{Ri}_B
ob.3d.B	[1.5, 2.7]	0.816	1.287	25.766±0.869	0.6	0.313	0.574	-1.095	21.8
"	[2.7, 5.5]	0.842	0.797	8.252±0.180	"	0.316	0.966	-1.616	36.0
"	[5.5, 8.0]	0.861	0.586	5.171±0.179	"	0.281	1.062	-1.789	50.0
ob.2d.c	[3.5, 5.7]	0.857	0.191	10.620±0.816	0.9	1.385	1.422	-2.154	5.9
ob.2d.C	[2.0, 4.0]	0.830	1.776	19.117±0.988	0.5	1.436	1.010	-1.887	3.2
ob.2d.e	[3.5, 8.0]	0.868	1.900	10.021±0.319	2.5	1.464	1.334	-2.289	4.4
ob.3d.B	[3.0, 8.0]	0.429	0.057	-0.700±0.009	0.50	0.479	30.686	-2.601	418.6
ob.2d.c	[3.5, 5.7]	0.428	0.201	-1.686±0.058	1.05	1.769	33.739	-2.811	86.3
ob.2d.C	[2.0, 4.0]	0.430	0.193	-1.625±0.072	0.65	1.434	32.160	-2.780	101.7
ob.2d.e	[3.5, 8.0]	0.429	0.162	-0.975±0.018	1.20	1.645	32.620	-2.879	84.4

^aThe rms fluctuations in the horizontal velocity at the interface location.

^bThe buoyancy jump across the interface.

 TABLE 6
 CONVECTIVE BOUNDARY LAYER PROPERTIES FOR "CORE CONVECTION" MODELS

Model	Time Interval (10^5 s)	\bar{r}_i (10^{11} cm)	\bar{h} (10^9 cm)	\bar{r}_i (10^3 cm/s)	$\overline{v_{exp}}^a$ (10^2 cm/s)	$\sigma[v_H]$ (10^5 cm/s)	$\overline{\Delta b}$ (10^2 cm/s ²)	$\log \bar{E}$	\overline{Ri}_B
msc.3d.B	[6.0, 10.0]	1.374	0.949	1.754± 0.080	...	2.011	6.07	-2.0594	66
"	[10.0, 12.0]	1.378	0.897	-0.020± 0.140	...	1.878	5.83	...	72
"	[12.0, 15.0]	1.382	0.998	2.731± 0.099	...	2.411	5.70	-1.9459	48
msc.2d.b	[6.0, 10.0]	1.369	1.319	1.401± 0.390	...	8.070	6.43	-2.7604	9.2

^aThe expansion velocity in these models remains very small with $v_{exp} < 10$ cm/s.